Master's Thesis 2026

Porous Rib Structure Optimization in Ultra-Thin Vapor Chambers

Chenzi Gao , Siqi Wu

ISSN: 0282-1990
ISRN: LUTMDN/TMHP-26/5694-SE

Department of Energy Sciences
LTH | Lund University

Master's Thesis

Sustainable Energy Engineering

Porous Rib Structure Optimization in Ultra-Thin Vapor Chambers

Chenzi Gao , Siqi Wu

Porous Rib Structure Optimization in Ultra-Thin Vapor Chambers

Chenzi Gao , Siqi Wu
chentsikao@gmail.com

June 12, 2026

Master's thesis work carried out at Lund University.

Supervisors: Himani Garg, himani.garg@energy.lth.se
Examiner: Martin Andersson, martin.andersson@energy.lth.se

Abstract

To manage increasing chip power densities in high-performance computing, vapor chambers have emerged as a leading passive cooling solution, but ultra-thin designs require support columns that obstruct vapor flow and compromise thermal uniformity. This thesis addresses how the number and arrangement of support ribs affect the coupled thermal-hydraulic behaviour. The primary goal was to develop a validated three-dimensional transient numerical model and use it to investigate the effect of rib number across multiple heat flux levels. The study is framed as a preliminary exploration of the design space rather than a formal optimization procedure, focusing specifically on the effect of rib number and arrangement while keeping rib thickness, cross-sectional shape, and spacing fixed. First, a no-rib baseline was simulated and confirmed to lose two-phase operation: lacking the parallel conduction paths and the auxiliary capillary return that the ribs provide, the evaporator superheats to roughly 197 °C and boils off the local liquid, yet the vapor never circulates or condenses back, so the chamber dries out. This verifies the necessity of support structures and validates the model's ability to capture this failure mode. Subsequently, a 12-rib, a 14-rib, and a symmetric 16-rib (4×4 matrix) configuration — the 12- and 14-rib layouts obtained by selectively removing non-critical ribs from the 16-rib baseline — were compared at heat fluxes of 80, 400, and 800 kW/m^2.

A key finding is that increasing the rib count does lower the peak temperature — at 400 kW/m^2 the peak wick temperature falls from approximately 164 ℃ for the 12-rib layout to 94 ℃ for 14 ribs and 44 ℃ for 16 ribs — but the vapor volume fraction reveals that this reduction is driven by a change of operating regime rather than by improved two-phase performance. At the same heat flux the vapor volume fraction drops from full saturation (VF ≈ 1.0, VC-12) through partial saturation (VF ≈ 0.88, VC-14) to essentially zero (VF ≈ 0.005, VC-16): the denser the rib array, the more the chamber reverts from phase-change-dominated operation towards pure solid conduction. The low temperature of the 16-rib layout therefore reflects a near-solid metallic spreader rather than an efficiently working vapor chamber. Selecting the rib count is thus a trade-off between mechanical support and preserving an active vapor phase at the design heat flux. For the 12-rib configuration, which remains an active vapor chamber across the tested range, a tentative operating window of approximately 200–600 kW/m^2 is suggested on the basis of the observed trends.

Keywords: MSc, Vapor chamber, Support ribs, Thermal management, Phase-change heat transfer, Computational fluid dynamics (CFD), Heat flux, Porous wick, Thermal resistance

Acknowledgments

This master's thesis was carried out at the Department of Energy Science in the spring of 2026, Faculty of Engineering (LTH), Lund University, Sweden, during the spring semester of 2026. The work was conducted as part of the Master's Programme in Energy Science and represents the culmination of our graduate studies at Lund University. The project was initiated in response to the growing demand for efficient thermal management solutions in high-performance computing applications, where rapidly increasing chip power densities have made conventional cooling approaches insufficient. Motivated by the critical role of anti-collapse support structures in ultra-thin vapor chamber design, and by the limited numerical understanding of porous rib configurations in such systems, this study was undertaken to bridge existing research gaps through systematic three-dimensional numerical analysis. We would like to express our sincere gratitude to our supervisor, Himani Garg, for her invaluable guidance, constructive feedback, and continuous support throughout the entire course of this project. Her expertise and encouragement were instrumental in shaping both the direction and quality of this work. We also extend our appreciation to our examiner, Martin Andersson, for his thoughtful review and insightful comments that helped strengthen the final thesis.

We would also like to clarify the individual contributions of the two authors to this thesis. Siqi Wu carried out the numerical simulations of the VC-N, VC-12, and VC-16 configurations, while Chenzi Gao was responsible for the VC-14 case. Prior to writing the thesis, both authors thoroughly discussed and jointly interpreted the simulation results. The manuscript was written by Chenzi Gao and subsequently reviewed and revised by Siqi Wu.

Nomenclature

Abbreviations

CFD	Computational Fluid Dynamics
CHF	Critical Heat Flux
HTC	Heat Transfer Coefficient
SoC	System-on-Chip
UTVC	Ultra-Thin Vapor Chamber
VC	Vapor Chamber
VF	Vapor Volume Fraction

Greek symbols

ΔP_{cap}	Capillary pressure
ΔP_{vc}	Total pressure drop across the vapor chamber
ΔT_c	Condenser-surface temperature non-uniformity
Δv	Specific volume change between phases
ε	Porosity of the porous structure
ε_l, ε_v	Liquid and vapor volume fractions
θ	Contact angle between liquid and solid surface
μ	Dynamic viscosity
ρ	Density
ρ_l, ρ_v	Liquid and vapor densities
σ	Surface tension of the working fluid

Variables

C_2	Inertial resistance coefficient
C_E	Ergun inertial coefficient
c_p	Specific heat at constant pressure
h_∞	Convective heat transfer coefficient
h_{fg}	Latent heat of vaporisation
K	Permeability of the porous medium
k	Thermal conductivity
$\dot{m}_e$, $\dot{m}_c$	Evaporation and condensation mass source terms
P	Pressure

P_{sat}	Saturation pressure
Q	Total heat input
q''	Heat flux
R_v	Specific gas constant of the vapor
R_{vc}	Overall thermal resistance of the vapor chamber
r_e, r_c	Evaporation and condensation intensity coefficients
r_{eff}	Effective pore radius of the wick
S_M	Momentum source term (body forces)
S_T	Volumetric energy source term (latent heat)
T	Temperature
T_{sat}	Saturation temperature
T_e, T_c	Evaporator and condenser surface temperatures
T_∞	Ambient temperature
t	Time
$\mathbf{V}$	Velocity vector

Subscripts

c	Condenser / condensation
e	Evaporator / evaporation
eff	Effective
l	Liquid phase
s	Solid phase
sat	Saturation
v	Vapor phase

Contents

Abstract vii

Acknowledgments ix

Nomenclature xi

1 Introduction . . . 1
- 1.1 Overview of Vapor Chambers and Support Rib Structures . . . 1
- 1.2 Literature Study . . . 3
- 1.3 Aim . . . 5

2 Theory . . . 6
- 2.1 Flow Parameters . . . 6
- 2.2 Heat Transfer and Phase Change . . . 7
- 2.3 Performance Evaluation Indicators . . . 9
- 2.4 Computational Fluid Dynamics . . . 10

3 Method . . . 10
- 3.1 Methodology Overview . . . 11
- 3.2 Computational Domain and Rib Configurations . . . 11
- 3.3 Boundary Conditions and Initial Conditions . . . 13
- 3.4 Meshing . . . 14
- 3.5 Numerical Setup . . . 15
- 3.6 Output Parameters . . . 16
- 3.7 Mesh Sensitivity Study . . . 17
- 3.8 Parametric Study Design . . . 17

4 Results . . . 18
- 4.1 Model Verification through the No-Rib Baseline . . . 18
- 4.2 Influence of Rib Configuration . . . 20
- 4.3 Detailed Per-Configuration Analysis . . . 26
- 4.4 Summary of Key Findings . . . 32

5 Discussion 36
5.1 Verification of the Model through the No-Rib Case 36
5.2 Influence of Rib Configuration 37
5.3 Influence of Heat Flux on Operating Regime 38
5.4 Comparison with the Reference Study 39
5.5 Limitations of the Numerical Methodology 41
6 Concluding Remarks 43
7 Perspectives 44

References **46**

1 Introduction

1.1 Overview of Vapor Chambers and Support Rib Structures

The vapor chamber is one of the most effective passive heat transfer devices used today, widely employed in electronics cooling for high-performance computing, consumer devices such as smartphones and laptops, server systems, LED lighting, and aerospace thermal management. Functionally similar to a flat heat pipe, the vapor chamber transfers heat through the continuous evaporation and condensation of a working fluid sealed within a vacuum-tight enclosure containing a capillary wick structure. The concept of a capillary-driven two-phase heat transfer device was first patented by Richard S. Gaugler of General Motors in 1942, but the design was not pursued further at the time [1]. It was not until 1963 that George M. Grover, working at the Los Alamos National Laboratory, independently developed the first working prototype and coined the term "heat pipe", which is widely regarded as the beginning of the modern heat pipe and its planar derivative, the vapor chamber [2]. With the rapid increase in chip power densities since the 2000s, ultra-thin vapor chambers have become a mainstream cooling solution in flagship smartphones and high-performance laptops [3].

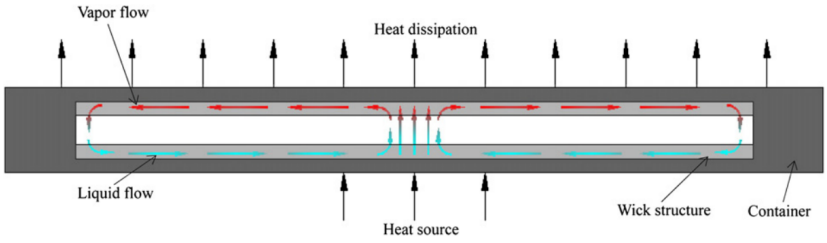


Figure 1: Schematic diagram of a vapor chamber and the associated flow mechanism [3]

The operating cycle of a vapor chamber consists of four sequential processes driven by capillary action and a vapor pressure gradient. The first step is evaporation, where heat from the source is absorbed by the working fluid (commonly water) saturating the wick above the heat source, causing it to vaporize and absorb a large amount of latent heat. The second step is vapor transport, where the generated vapor flows from the evaporator region to the cooler condenser region through the central vapor core, driven by a small pressure differential between the two zones. The third step is condensation, where the vapor releases its latent heat on the condenser surface and returns to the liquid phase. The final step is capillary return, where the condensed liquid is drawn back to the evaporator through the porous wick structure by capillary forces, completing the cycle without any external pumping power [4]. This closed two-phase cycle allows vapor chambers to achieve effective thermal conductivities up to two orders of magnitude higher than that of solid copper [2].

The operation of a vapor chamber involves the coupled interaction of conduction, convection, two-phase change, and capillary-driven flow in a porous medium, each governed by classical heat transfer theory. Within the porous wick, liquid transport is driven by capillary pressure described by the Young–Laplace equation [4]:

$$\Delta P_{cap} = \frac{2\sigma \cos\theta}{r_{eff}} \tag{1}$$

where σ is the surface tension of the working fluid, θ the contact angle, and r_{eff} the effective

pore radius. The phase-change process at the liquid–vapor interface is anchored by the Clausius–Clapeyron relation, which links the local saturation pressure to the saturation temperature through the latent heat of vaporisation h_{fg} and the specific volume change Δv between phases [10]:

$$\frac{\mathrm{d}P_{sat}}{\mathrm{d}T_{sat}} = \frac{h_{fg}}{T_{sat}\,\Delta v} \tag{2}$$

Finally, the overall thermal performance is characterised by the equivalent thermal resistance:

$$R_{vc} = \frac{T_e - T_c}{Q} \tag{3}$$

where T_e and T_c are the evaporator and condenser surface temperatures and Q is the total heat input.

Over the past two decades, vapor chamber technology has evolved rapidly, driven by the demand for thermal management in increasingly compact and powerful electronic devices. In the early 2000s, vapor chambers were primarily used in server CPUs and high-end desktop processors, with typical thicknesses ranging from 3 to 5 mm and footprint areas of around 50 × 50 mm² [5]. With the rise of smartphones and ultra-thin laptops after 2010, ultra-thin vapor chambers (UTVCs), generally defined as those with a total thickness below 2.0 mm, became a major research focus [6]. By the late 2010s, mainstream flagship smartphones such as the Xiaomi Mi 11 Ultra and Samsung Galaxy Z Fold series began adopting copper vapor chambers with thicknesses below 0.4 mm and surface areas exceeding 4000 mm², capable of dissipating sustained heat loads of 10–15 W from chips such as the Snapdragon 888 [7]. More recently, UTVCs with thicknesses as low as 0.3 mm and even 0.32 mm have been successfully demonstrated through advanced manufacturing processes, including precision etching of integrated capillary structures and optimised second-vacuuming sealing techniques [8] [9]. In terms of cooling efficiency, modern UTVCs can achieve effective thermal conductivities of up to 20,900 W/(m·K) in horizontal orientation, approximately 52 times higher than that of pure copper, with thermal resistances reaching as low as 0.035 K/W under forced convection cooling [6] [10]. Despite these advances, several technical

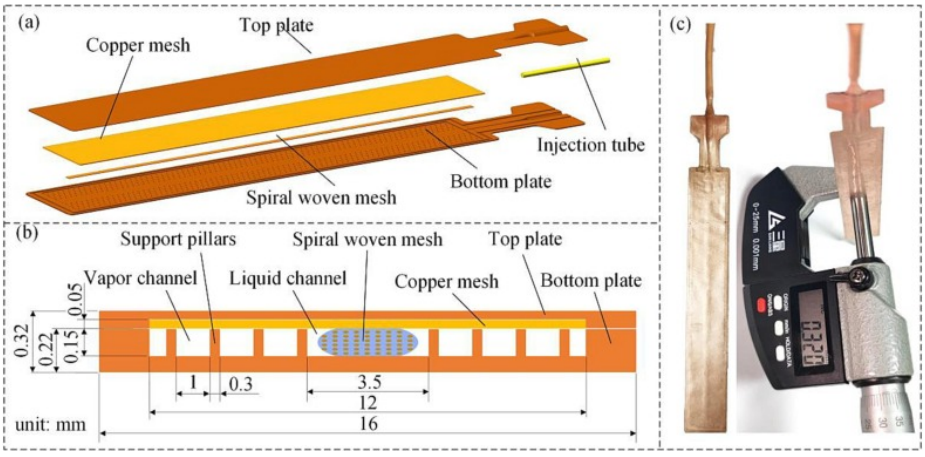


Figure 2: Structure and dimensions of UTVC: (a) scheme diagram of UTVC components; (b) Cross section structure and dimensions of UTVC; (c) Photograph of final UTVC sample [8]

bottlenecks continue to constrain further development. The most fundamental limitation is the trade-off between thickness and heat transfer capacity: as the internal vapor cavity becomes thinner, the cross-section available for vapor flow shrinks, sharply increasing

flow resistance and reducing the maximum heat transport capacity. This effect becomes particularly severe when the internal cavity thickness falls below 0.3 mm, where the total thermal resistance rises rapidly [6]. A second bottleneck arises from the coupled limitation of capillary force and liquid return: smaller wick pore sizes generate stronger capillary pressure but simultaneously increase the viscous flow resistance of the returning liquid, leading to dryout at the evaporator when chip power exceeds a critical threshold [4]. A third challenge concerns mechanical integrity, as ultra-thin enclosures are susceptible to collapse under internal vacuum and external clamping forces, necessitating internal support structures such as ribs or columns that inevitably obstruct vapor flow and create local hotspots [11]. Additional issues include non-condensable gas accumulation that degrades long-term performance, manufacturing inconsistencies in capillary uniformity and sealing quality at mass-production scale, and the intrinsic property limits of water as the dominant working fluid, which restrict operation to roughly 100 °C and degrade startup performance at low ambient temperatures [8] [12].

The present study targets the thermal management of high-performance computing processors in compact devices such as flagship smartphones, tablets, and ultra-thin laptops, where the system-on-chip generates highly concentrated heat over a small footprint while the available package thickness is severely constrained. This application context motivates the parameter choices adopted throughout this work: the 20×20 mm heat source represents a typical mobile SoC die area, and the three heat flux levels of 80, 400 and 800 kW/m^2 span the range from sustained nominal operation to short-duration peak loads characteristic of such chips. Anchoring the study to this application makes the selected geometry and operating window directly comparable to the conditions faced by real ultra-thin vapor chambers in consumer electronics.

1.2 Literature Study

Despite the growing demand for high-performance vapor chambers in electronics cooling, systematic numerical studies on internal support structures remain relatively limited in the open literature. Vapor chamber modelling has evolved from early simplified one-dimensional thermal resistance networks into high-fidelity three-dimensional steady-state and transient models. Early models often simplified the vapor core as an isothermal layer in pursuit of computational efficiency, but struggled to accurately capture local thermal characteristics under high heat flux conditions.

In 2009, Chen et al. [13] demonstrated that for system-level simulations, simplifying the vapor core as a shared heat transfer interface is a practical and feasible approach for predicting the performance of integrated heat sinks, providing one of the early frameworks balancing accuracy and computational cost.

In 2012, Ranjan et al.[14] utilised kinetic theory based on the Hertz–Knudsen equation in combination with the Clausius–Clapeyron equation to compute the interfacial mass flux, applying it to the prediction of thin-film evaporation processes. This work provided one of the earliest detailed treatments of phase change at the liquid–vapor interface in vapor chamber CFD.

In 2023, Rahmatullah and Wen [15] proposed an efficient scheme using the Ghost Fluid Method to apply mass and energy source terms based on the Lee model to a single-phase flow field, without requiring the interface to be predefined as either evaporating or condensing, significantly enhancing numerical stability. Rahmatullah also emphasised that,

under high-power operating conditions, the ideal gas equation of state must be coupled to account for vapor compressibility, rather than relying on the traditional incompressible assumption used in earlier studies.

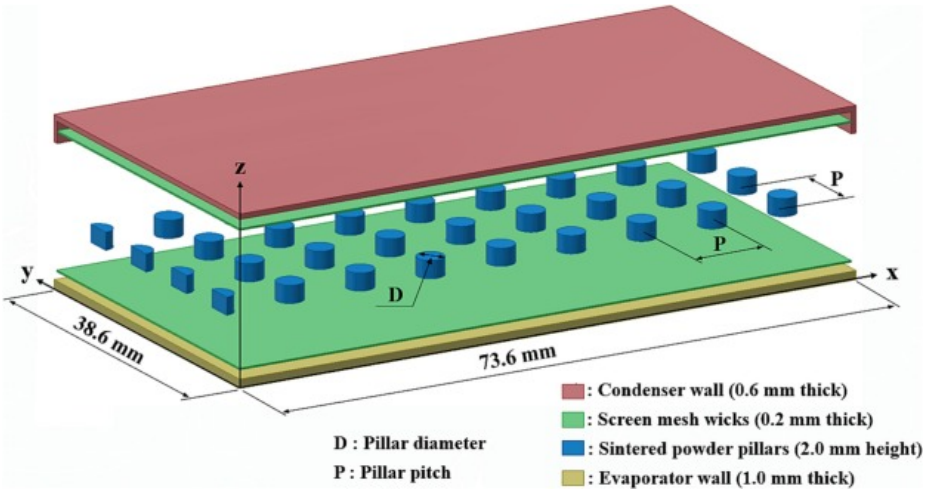


Figure 3: The schematic of the quarter 3D vapor chamber model. The pillar diameter and pitch are factors of interest [16]

In 2024, R. Li et al. [8] conducted a three-dimensional transient CFD study on mesh-type ultra-thin vapor chambers, partitioning the computational domain into solid walls, porous wick, and vapor core. To describe liquid flow through the microstructure, the Brinkman–Forchheimer extended Darcy model was adopted to balance viscous resistance with inertial losses, and an anisotropic effective thermal conductivity formulation was introduced to account for directional heat conduction within the woven mesh. Li also incorporated the Marangoni effect, treating the surface tension gradient induced by temperature gradients as a shear-stress boundary condition in the momentum equation, and concluded that this effect noticeably influences liquid return in sub-millimeter designs.

Also in 2025, Xie et al. [17] applied Hertz–Knudsen kinetic theory at the phase-change interface to analyse supporting-column ultra-thin vapor chambers with graded microgrooves, evaluating the contribution of gradient capillary structures to enhancing the heat transfer limit. The study further reflected a broader research trend in anti-collapse structures, which has shifted from purely solid support pillars towards composite support structures (solid core with porous outer layer) coupled with graded capillary force networks.

Similarly, in 2025, Sudhakar et al. [18] addressed the limitations of conventional single-phase evaporation models at heat fluxes exceeding 100 W/cm². They pointed out that neglecting boiling inside the wick severely overestimates the dryout limit, and developed a two-phase flow physical model accounting for vapor–liquid coexistence, using relative permeability and liquid saturation to correct the pressure field and thereby accurately predict the dryout heat flux.

Most recently, Jiang et al. [19] employed a three-dimensional transient model to analyse the thermal behaviour of electronic devices under fluctuating loads, solving the dynamic evolution of temperature, pressure, and flow velocity over time. To reduce computational cost, the model exploited geometric symmetry and discretised only a quarter or half of the full domain. The mainstream modelling approach adopted in this and similar studies partitions the computational domain into three functional regions: the solid region, where

Fourier-based heat conduction equations are applied to the shell and support pillars; the wick region, governed by the Brinkman–Forchheimer extended Darcy model; and the vapor core, where the Navier–Stokes equations are solved for the flow field.

While these studies have advanced the numerical understanding of vapor chamber operation, systematic investigations of rib-type porous supports — in particular the effect of rib number and arrangement — remain scarce. Existing work has primarily focused on cylindrical support pillars or overall wick optimisation, leaving the influence of rib-type structures on vapor flow and temperature uniformity largely unexplored. This thesis addresses this gap by systematically examining the effect of rib number and arrangement at a fixed square cross-section, while rib thickness and cross-sectional shape are left to future work.

1.3 Aim

This thesis focuses on porous rib structures in ultra-thin vapor chambers, and is divided up into two sub-goals.

The first goal is to develop and validate a three-dimensional transient CFD methodology specifically for ultra-thin vapor chambers with porous support structures. This involves investigating the meshing strategy, phase-change interface treatment, and boundary conditions to find a numerical method capable of accurately predicting the temperature, pressure, and vapor velocity distributions within the chamber. To support this, the methodology also includes an investigation into key flow and heat transfer characteristics such as the evaporation–condensation cycle, vapor flow around support structures, and capillary-driven liquid return, which are fundamental to the cooling performance. This is done based on an initial literature review and testing of the Lee phase-change model coupled with the Brinkman–Forchheimer extended Darcy model for porous wick flow, and validating against a no-column baseline case to confirm that the model correctly captures dryout behaviour.

The second goal is to investigate the influence of porous rib configurations on vapor chamber performance. Using the validated CFD methodology, this part of the study will analyse how varying the number, arrangement, and operating heat flux of support columns affects the thermal-hydraulic performance of the system. The key metrics for this investigation will be the changes in thermal resistance, condenser surface temperature uniformity, and vapor core pressure drop, evaluated across three representative heat flux levels.

1.3.1 Delimitations

Due to computational limitations, the model domain will be simplified compared to what would be used in an actual electronic device. The study will use a symmetric quarter-domain representation, which, due to time constraints, may not fully capture asymmetric flow behaviour that could arise in full-scale geometries. To minimise complexity, the analysis will not consider non-condensable gas accumulation, manufacturing-induced wick non-uniformity, or working-fluid degradation effects. The primary focus of this investigation is on determining the thermal resistance, temperature uniformity, and pressure drop, and the subsequent identification of an optimised support column configuration.

2 Theory

In the theory chapter, a quick overview of the governing equations, porous-media flow modelling, phase-change formulation, and performance evaluation indicators relevant to ultra-thin vapor chamber simulation is presented. A brief description of the numerical framework used in this thesis is given at the end.

2.1 Flow Parameters

2.1.1 Governing Equations

The governing equations of fluid flow are mathematical formulations of the three conservation laws of physics. At the length scales relevant to vapor chamber simulation, the fluid can be treated as a continuous medium, and the molecular structure of the working fluid may be ignored [20].

The conservation of mass states that the rate of increase of mass in a fluid element must equal the net rate of mass flow into the element. For a compressible fluid this yields:

$$\frac{\partial \rho}{\partial t} + \nabla \cdot (\rho \mathbf{V}) = 0 \tag{4}$$

where ρ is the fluid density, t is time, and $\mathbf{V}$ is the velocity vector.

The momentum equation is a formulation of Newton's second law. For a Newtonian fluid, the three-dimensional Navier–Stokes equation can be written as:

$$\frac{\partial (\rho \mathbf{V})}{\partial t} + \nabla \cdot (\rho \mathbf{V}\mathbf{V}) = -\nabla P + \nabla \cdot (\mu \nabla \mathbf{V}) + \mathbf{S}_M \tag{5}$$

Where P is the static pressure, μ is the dynamic viscosity, and S_M represents body forces, which in this work account for gravity acting on the working fluid. [20].

The three-dimensional energy equation describes the transport of internal energy through convection, conduction, and source terms:

$$\frac{\partial (\rho c_p T)}{\partial t} + \nabla \cdot (\rho c_p \mathbf{V} T) = \nabla \cdot (k \nabla T) + S_T \tag{6}$$

where c_p is the specific heat at constant pressure, T is the temperature, k is the thermal conductivity, and S_T is a volumetric heat source term used to account for the latent heat released or absorbed during phase change [21].

2.1.2 Flow in Porous Media

The wick layer and porous support ribs cannot be treated as a free flow domain because their solid skeleton imposes additional viscous and inertial resistances on the liquid. For the moderate-permeability range typical of sintered powders and woven meshes used in vapor chambers, the Brinkman–Forchheimer extended Darcy model is widely adopted [22, 23].

This model extends classical Darcy flow by retaining the viscous shear term (the Brinkman correction) and adding a quadratic inertial loss term (the Forchheimer correction):

$$\frac{\rho}{\varepsilon}\frac{\partial \mathbf{V}}{\partial t} + \frac{\rho}{\varepsilon^2}(\mathbf{V}\cdot\nabla)\mathbf{V} = -\nabla P + \frac{\mu}{\varepsilon}\nabla^2\mathbf{V} - \frac{\mu}{K}\mathbf{V} - \frac{C_E\rho}{\sqrt{K}}|\mathbf{V}|\mathbf{V} \tag{7}$$

where ε is the porosity of the porous structure, K is the permeability, and C_E is the Ergun inertial coefficient, commonly determined from $C_E = 1.75/\sqrt{150\varepsilon^3}$ [24]. Smaller pore sizes increase the capillary driving force but simultaneously raise the viscous resistance through reduced permeability, forming one of the fundamental trade-offs in wick design.

In the vapor core, no porous-medium treatment is applied; the region is modeled directly as a fluid domain. The momentum source term therefore drops out, and the above equation reduces to the standard Navier–Stokes form.

2.1.3 Vapor Compressibility

Under high heat flux conditions, when the chamber operates in a fully active two-phase regime, the vapor velocity inside ultra-thin chambers can become large enough that compressibility effects are no longer negligible. Following the approach proposed by Rahmatullah and Wen [15], the vapor density in this work is computed from the ideal gas law:

$$\rho_v = \frac{P}{R_v T} \tag{8}$$

where R_v is the specific gas constant of the vapor. This treatment replaces the conventional incompressible assumption used in early vapor chamber models and is essential for accurate prediction at heat fluxes above approximately 100 kW/m^2.

It should be noted that this compressible treatment is retained as a conservative choice that remains valid across all operating regimes: it is strictly necessary only in the high-flux, fully active cases where the vapor attains velocities on the order of metres per second, whereas in the conduction-dominated regimes the vapor throughflow is negligible and the compressibility correction has no appreciable effect. Adopting the ideal-gas formulation throughout therefore introduces no error in the low-speed cases while correctly capturing compressibility where it matters.

2.2 Heat Transfer and Phase Change

2.2.1 Conduction in Solid Walls and Wick

Conductive heat transfer in the solid aluminium walls and through the saturated wick layer is described by Fourier's law of heat conduction [21]:

$$q'' = -k\nabla T \tag{9}$$

where q'' is the local heat flux and k is the thermal conductivity. Within the wick, the effective volumetric heat capacity and effective thermal conductivity are determined by volume-weighted averaging of the liquid and solid phases:

$$(\rho c_p)_{\text{eff}} = \varepsilon\,(\rho c_p)_l + (1-\varepsilon)\,(\rho c_p)_s \tag{10}$$

$$k_{\text{eff}} = \varepsilon\,k_l + (1-\varepsilon)\,k_s \tag{11}$$

where subscripts l and s denote the liquid and solid phases respectively. This volume-averaged treatment is standard practice for porous wick modelling and provides adequate accuracy when the pore-scale temperature variation is small compared to the macroscopic gradient [4]. For the porous wick and the support ribs, the solid phase (s) is copper, whereas the solid envelope walls are treated as aluminium and modelled with the single-phase form of Fourier's law (Equation 9) using the material properties listed in Table 1.

Table 1: Thermophysical properties used in the simulation.

Material	ρ (kg/m^3)	c_p (J/kg·K)	k (W/m·K)
Aluminium (wall)	2719	871	202.4
Copper (wick/ribs)	8978	381	387.6
Liquid (water)	998	4182	0.6
Vapor (water)	ideal gas	2080	0.025

2.2.2 Capillary Pressure in the Wick

Within the porous wick, liquid transport from the condenser back to the evaporator is driven by capillary pressure described by the Young–Laplace equation [4]:

$$\Delta P_{cap} = \frac{2\sigma\cos\theta}{r_{eff}} \tag{12}$$

where σ is the surface tension of the working fluid, θ is the contact angle between the liquid and the solid surface, and r_{eff} is the effective pore radius of the wick. The capillary pressure must overcome the combined liquid and vapor pressure drops along the flow path; once the maximum capillary pressure is insufficient to sustain the required liquid return rate, the wick dries out at the evaporator, marking the capillary limit of operation [12].

2.2.3 Phase Change at the Liquid–Vapor Interface

The relationship between the saturation pressure and saturation temperature at the liquid–vapor interface is governed by the Clausius–Clapeyron relation [21]:

$$\frac{\mathrm{d}P_{sat}}{\mathrm{d}T_{sat}} = \frac{h_{fg}}{T_{sat}\,\Delta v} \tag{13}$$

where h_{fg} is the latent heat of vaporisation and Δv is the specific volume change between the liquid and vapor phases. For water at moderate operating temperatures, the large value of h_{fg} (approximately 2260 kJ/kg at atmospheric pressure) is the primary reason vapor chambers achieve effective thermal conductivities orders of magnitude higher than solid copper.

To incorporate phase change into the CFD framework, the Lee model is adopted in this work [25]. The Lee model treats evaporation and condensation as volumetric mass source terms proportional to the local deviation of temperature from the saturation temperature:

$$\dot{m}_e = r_e \rho_l \varepsilon_l \frac{T - T_{sat}}{T_{sat}}, \qquad T > T_{sat} \tag{14}$$

$$\dot{m}_c = r_c \rho_v \varepsilon_v \frac{T_{sat} - T}{T_{sat}}, \qquad T < T_{sat} \tag{15}$$

where r_e and r_c are the evaporation and condensation intensity coefficients, ρ_l and ρ_v are the liquid and vapor densities, and ε_l, ε_v are the corresponding volume fractions. The latent heat associated with phase change is included as an energy source term applied at the interface cells:

$$S_T = \dot{m} h_{fg} \tag{16}$$

The choice of r_e and r_c influences numerical stability and the sharpness of the predicted interface; typical values reported in the literature range from 0.1 to 100 s^{-1}, with smaller values producing smoother but slower convergence. [26] [27]

2.3 Performance Evaluation Indicators

Three key indicators are used in this thesis to quantify the thermal-hydraulic performance of different rib configurations. These indicators are defined here and used consistently in the results chapter.

The overall thermal resistance of the vapor chamber represents the total opposition to heat flow from the evaporator to the condenser and is defined as [4]:

$$R_{vc} = \frac{T_e - T_c}{Q} \tag{17}$$

where T_e and T_c are the average temperatures of the evaporator and condenser surfaces respectively, and Q is the total heat input. A lower R_{vc} indicates more efficient heat spreading.

Condenser temperature uniformity is characterised by the maximum temperature difference across the condenser surface, which directly reflects the severity of local hotspots:

$$\Delta T_c = T_{c,\max} - T_{c,\min} \tag{18}$$

A small ΔT_c is particularly important for cooling chips with non-uniform power maps, as it determines the worst-case junction temperature seen by the device.

The total pressure drop across the vapor chamber, which must remain below the capillary pressure limit of the wick to avoid dry-out, is given by:

$$\Delta P_{vc} = \Delta P_l + \Delta P_v \tag{19}$$

where ΔP_l and ΔP_v are the maximum liquid and vapor pressure drops respectively.

2.4 Computational Fluid Dynamics

As of writing there is no analytical solution to the coupled set of governing equations described above for a general three-dimensional vapor chamber geometry. Numerical solvers are therefore used to approximate the real-world thermal-hydraulic behaviour [20]. The CFD methodology in this work is structured around three main stages: pre-processing (geometry, mesh, boundary conditions, physical models), solving (numerical approximation of the governing equations over the discretised domain), and post-processing (visualisation and analysis of results).

2.4.1 Transient Solution Framework

In contrast to most prior vapor chamber CFD studies that adopt a steady-state formulation, this work solves the governing equations in transient form. The motivation is two-fold: first, the startup transient from ambient temperature to fully developed vapor flow contains physically important information about phase-change initiation and dryout onset; second, transient simulation provides better numerical stability when the phase-change source terms are stiff, as the small physical time step naturally limits the change in interfacial mass flux per iteration.

A first-order implicit scheme is used for time integration. For spatial discretisation, a second-order upwind scheme is applied to the convective terms and central differencing to the diffusive terms, consistent with established practice in two-phase CFD [28].

2.4.2 Phase-Change Coupling Strategy

The Lee-model mass and energy source terms are handled by the built-in evaporation–condensation model in ANSYS Fluent and evaluated at each time step. At every iteration, the solver computes the local temperature deviation from the saturation temperature, evaluates the mass transfer rate, and applies the corresponding source terms to the continuity and energy equations of the interface cells. The saturation temperature is held fixed at the operating saturation value throughout the simulation, consistent with the fixed-saturation-temperature assumption adopted in this work.

Steady state is considered to be reached when the difference between the heat input at the evaporator and the heat output at the condenser falls within 2%, in line with the convergence criterion proposed by Rahmatullah and Wen [15].

3 Method

In this chapter, the method of the thesis is presented. An overview of the computational domain, support rib geometries, boundary conditions, meshing process, and numerical setup is given. The output parameters used for the results in the next chapter are also described.

3.1 Methodology Overview

The CFD workflow consisted of three main stages: pre-processing, simulation, and post-processing. The following tools were used in the method of this thesis work.

- **ANSYS DesignModeler** – used for all geometry creation.
- **ANSYS Discovery** – used for visualisation and figure generation of the computational domain.
- **Fluent Meshing** – used to generate the hybrid mesh.
- **ANSYS Fluent** – CFD software used for all transient simulations, including the Lee phase-change model applied through Fluent's built-in evaporation–condensation model. The built-in post-processing functionality of Fluent was also used for extracting contour plots, vector fields, and streamlines.
- **Microsoft Excel** – used for data processing, tabulation, and plotting of transient curves and performance comparisons.

3.2 Computational Domain and Rib Configurations

3.2.1 Vapor Chamber Geometry

The vapor chamber consists of four functional zones stacked vertically: the solid aluminium walls, the porous liquid wicks on the upper and lower walls, the porous support ribs, and the central vapor core. The outer dimensions and layer thicknesses used in this work are based on a representative ultra-thin vapor chamber for high-performance computing applications, and are summarised in Table 2.

Table 2: Geometric parameters of the vapor chamber.

Region	Length [mm]	Width [mm]	Thickness [mm]
Solid wall (full envelope)	100	100	4.0
Wick layer (upper and lower)	90	90	2.0 (1.0 each side)
Vapor core	89	89	1.0

To reduce computational cost while preserving physical accuracy, symmetry conditions are applied on two orthogonal vertical planes and only one quarter of the full geometry is modelled. A schematic of the quarter-domain layered structure is shown in Figure 4 and Figure 5.

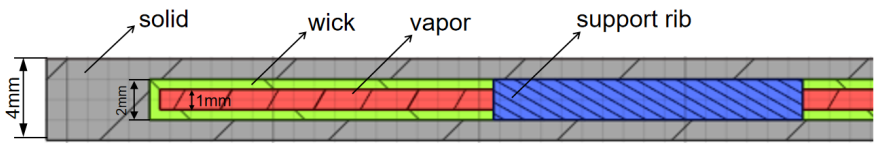


Figure 4: Layered structure of the 4×4-rib vapor chamber and the modelled quarter-domain.

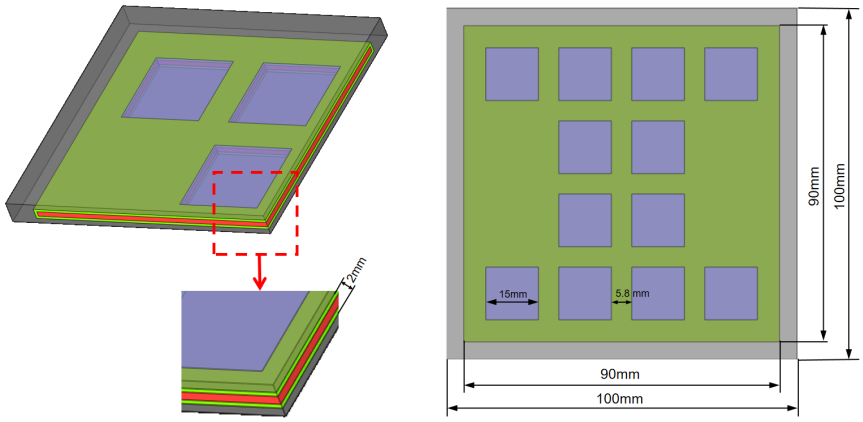


Figure 5: Top and side views of the vapor chamber with overall and rib dimensions (envelope 100×100 mm, rib side 15 mm, rib spacing 5.8 mm).

3.2.2 Support Rib Configurations

Four support rib configurations are constructed to compare the effect of rib number and arrangement on vapor chamber performance.

VC-16 uses 16 square ribs arranged in a 4×4 matrix and serves as the baseline for a regular symmetric layout. **VC-12** is derived from VC-16 by removing four non-critical ribs to widen the central vapor channel while preserving the load-bearing ribs closest to the heat source. **VC-14** is an intermediate configuration with two ribs removed. **VC-N** contains no support ribs and is used to verify that support structures are mechanically and thermally indispensable.

All configurations share the same outer dimensions, wall thickness, wick thickness, and vapor core height. Only the number and arrangement of support ribs differ between cases, so that the comparisons isolate the effect of rib layout. The ribs in this study have square cross-sections with side length **15 mm**, an edge-to-edge spacing of **5.8 mm**, and a height equal to the vapor core height of 1.0 mm. With this layout the 4×4 array fills the 89 mm vapor core span uniformly (four 15 mm ribs separated and bordered by five 5.8 mm gaps). The schematic of each configuration is shown in Figure 6.

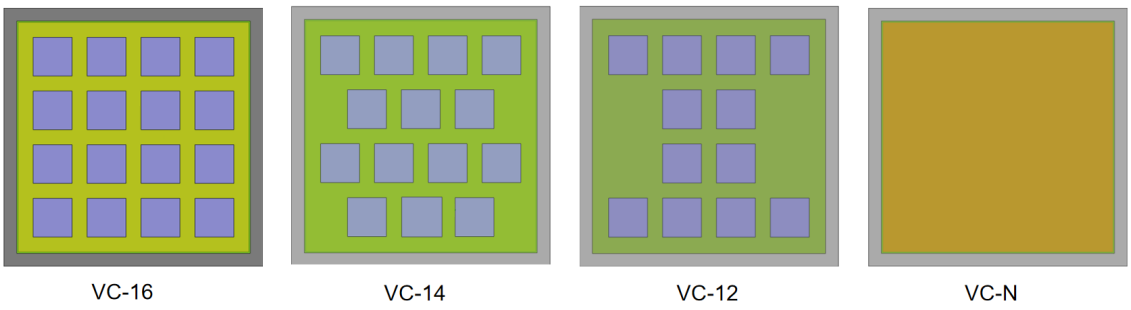


Figure 6: Top-view comparison of the four support rib configurations (VC-16, VC-14, VC-12, VC-N). Dashed outlines indicate the ribs removed from the baseline VC-16 layout.

The support ribs are modelled as porous copper structures sharing the same solid skeleton

material as the main wick but with a higher permeability ($K = 1.0 \times 10^{-8}$ m^2 versus 2.0×10^{-11} m^2 for the wick), forming a continuous capillary network that simultaneously provides mechanical reinforcement against vacuum-induced collapse and assists liquid return from the condenser to the evaporator.

3.3 Boundary Conditions and Initial Conditions

Three types of thermal boundary conditions are applied on the exterior walls of the quarter-domain, as illustrated in Figure 7.

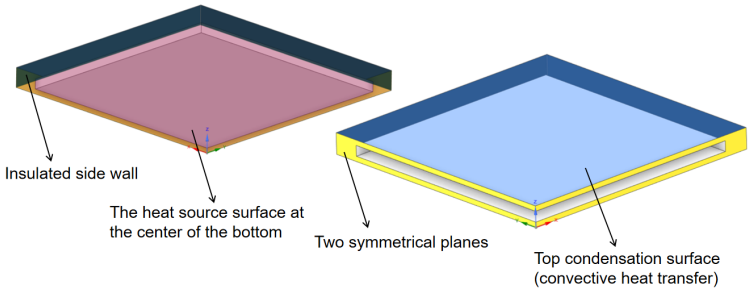


Figure 7: Thermal boundary conditions on the quarter-domain: heat-flux source on the evaporator wall, convective cooling on the condenser wall, adiabatic outer walls, and two symmetry planes.

A uniform heat flux q'' is imposed on a centred square heat source at the bottom of the evaporator-side wall to simulate chip-level heat input. The heat source has an in-plane footprint of 20×20 mm^2. Three representative heat flux levels are investigated: 80 kW/m^2 (low load), 400 kW/m^2 (medium load), and 800 kW/m^2 (near-critical load).

A convective boundary condition with heat transfer coefficient $h_\infty = 5000$ W/(m^2 K) and ambient temperature $T_\infty = 26.85\,°\text{C}$ is applied to the condenser-side top wall to represent the external cooling.

All remaining exterior surfaces, including the lateral side walls outside the heat source region, are treated as adiabatic. Symmetry conditions are imposed on the two symmetry planes of the quarter-domain.

The system is initialised at a uniform temperature equal to the ambient temperature, and the saturation temperature inside the vapor chamber is fixed at $T_{sat} = 50$ ℃ throughout the simulation. The initial operating pressure is set to the saturation pressure corresponding to 50 ℃, approximately 12.35 kPa.

The entire flow field is treated as laminar throughout, since the low vapor velocities and the small characteristic length scales of the ultra-thin chamber keep the flow well within the laminar regime. The two-phase transport of the working fluid—liquid water and its vapor—is resolved using the Mixture multiphase model, in which the two phases share a single set of momentum equations and are treated as interpenetrating continua. At initialisation the chamber is taken to be entirely filled with liquid water, and the transition between the liquid and vapor phases during operation is driven by an evaporation–condensation mechanism, implemented through the Lee model described in Section 3.5.

3.4 Meshing

A hybrid mesh is generated using Fluent Meshing to discretise the quarter-domain. The mesh combines structured hexahedral cells in regions with regular geometry (the bulk of the solid wall, wick, and vapor core) with prismatic or tetrahedral elements in regions surrounding the support ribs, where the geometry is locally complex.

Local refinement is applied in two critical regions to capture steep gradients accurately. The first refined region is the liquid–vapor interface between the wick and the vapor core, where the phase-change source terms are non-zero and large temperature gradients are expected. The second refined region surrounds each support rib, where vapor flow separation and wake formation occur. The overall mesh and the refined regions are shown in Figures 8 and 9.

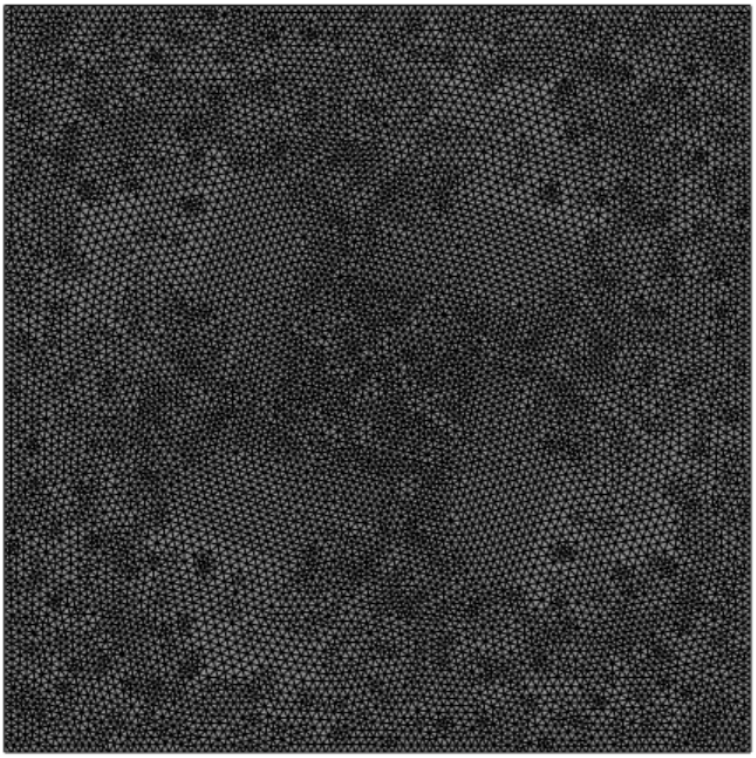


Figure 8: Overall hybrid mesh of the quarter-domain.

The cell size and growth rate used in the final mesh are summarised in Table 3.

Table 3: Mesh refinement settings.

Parameter	Value
Global base cell size	1.0 mm
Growth rate	1.2
Total cell count (VC-16)	102181

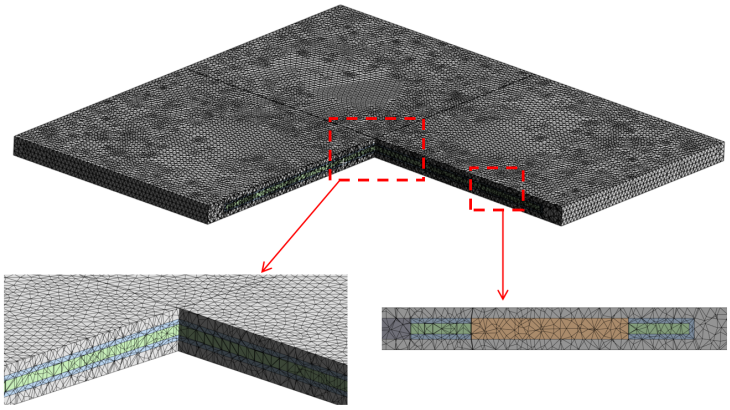


Figure 9: Close-up of the local mesh refinement at the liquid–vapor interface and around a support rib.

3.5 Numerical Setup

The governing equations are solved in transient form using **ANSYS Fluent**. The working fluid is water, with saturated liquid and vapor properties evaluated at the operating saturation temperature of 50 °C. The vapor phase is treated as compressible following the ideal gas law, while the liquid phase is assumed to be incompressible.

The porous wick and porous support ribs are modelled using the Brinkman–Forchheimer extended Darcy formulation. The porosity and permeability values used in this study are summarised in Table 4.

Table 4: Porous-medium properties used for the wick and support ribs.

Region	**Porosity** ε [–]	**Permeability** K [m^2]	**Inertial resistance** C_2 [m^{-1}]
Wick zone	0.4	2.0×10^{-11}	69872
Support ribs	0.3	1.0×10^{-8}	69872

It should be noted that the capillary pressure described by the Young–Laplace equation is not imposed as an explicit boundary condition in the present model. Instead, the liquid-return resistance of the porous wick and ribs is represented through the permeability K and inertial resistance C_2 of the Brinkman–Forchheimer extended Darcy formulation (Table 4), while the driving force for liquid return arises implicitly from the pressure field computed by the solver. Because no dedicated measurements of the contact angle, effective pore radius, or maximum capillary pressure were available for the modelled structures, these microscopic parameters are subsumed into the macroscopic porous-medium properties rather than prescribed individually. This is a common simplification in macroscale vapor-chamber CFD, and the capillary limit is instead monitored indirectly through the onset of dryout, as demonstrated in the no-rib (VC-N) verification case.

The solid envelope walls are modelled as aluminium, while the solid skeleton of both the porous wick and the support ribs is modelled as copper. The viscous resistance ($1/K$) values are 5×10^{10} and 1×10^{8} m^{-2} for the wick and the ribs respectively (corresponding to $K = 2.0 \times 10^{-11}$ and 1.0×10^{-8} m^2); together with the inertial resistance of 69872 m^{-1}, these are empirical values adopted from the range commonly reported in the open literature, as

no dedicated permeability measurements were available in this study.

The Lee phase-change model is applied using the built-in evaporation–condensation model in ANSYS Fluent. At each time step, the solver computes the local temperature deviation from the saturation temperature, evaluates the evaporation and condensation mass transfer rates, and applies the corresponding mass and energy source terms to the continuity and energy equations. The evaporation and condensation intensity coefficients are set to $r_e = r_c = 0.1\ \mathrm{s}^{-1}$, chosen to balance numerical stability with sharp interface resolution.

A pressure-based coupled solver is used. The default Fluent under-relaxation factors are retained. For spatial discretisation, a second-order upwind scheme is applied to the convective terms and central differencing to the diffusive terms. A first-order implicit scheme is used for time integration with a fixed time step of $\Delta t = 0.1$ s. Each simulation is run from $t = 0$ until steady state is reached, defined as the moment at which the difference between the heat input at the evaporator and the heat output at the condenser falls within 2%. The total simulated physical time is approximately **20 s**.

Gravity is included in this study through the body-force term in the momentum equation, with a gravitational acceleration of $9.81\ \mathrm{m/s}^2$, allowing orientation-dependent buoyancy and liquid-return effects to be captured.

3.6 Output Parameters

For each simulation, three primary performance indicators are extracted from the steady-state results, as defined in Section 2.3: the overall thermal resistance R_{vc}, the condenser surface temperature uniformity ΔT_c, and the total pressure drop across the vapor core ΔP_{vc}.

In addition to these scalar indicators, the following spatial fields are extracted for qualitative analysis:

- Steady-state wall temperature, wick temperature, and vapor core temperature distributions.
- Diagonal cross-section temperature contours.
- Vapor volume fraction (VF) distribution, used to identify regions of phase change and potential dryout.
- Steady-state pressure distribution along a diagonal cross-section.
- Steady-state vapor velocity vector field, used to identify bluff-body wake effects around support ribs.

Transient evolution of the maximum and minimum values of temperature and vapor volume fraction is also monitored throughout the simulation to identify the time required to reach steady state and to detect any non-physical behaviour during the startup transient. Convergence in this study is determined by the stabilisation of these key engineering quantities, in addition to the residual targets set in Fluent.

3.7 Mesh Sensitivity Study

A grid independence study was performed using the VC-16 configuration at the medium heat flux of 400 kW/m^2 to verify that the chosen mesh resolution produces a mesh-independent solution. Six meshes were generated by progressively refining the global base cell size while keeping the local refinement strategy (interface and support-rib sizing) identical between meshes. For each mesh the steady-state reference temperature (the characteristic evaporator-side temperature) was monitored as the convergence indicator. The resulting cell counts and reference temperatures are summarised in Table 5.

Table 5: Mesh sensitivity study results for VC-16 at 400 kW/m^2.

Mesh	Cell count	Reference temperature [°C]	R_{vc} [K/W]
M1 (coarsest)	20,000	42.3	0.0041
M2	57,000	48.0	0.0034
M3 (selected)	102,181	47.3	0.0032
M4	240,000	47.4	0.0032
M5	365,000	47.7	0.0032
M6 (finest)	485,000	47.6	0.0031

The reference temperature changes sharply between the two coarsest meshes but stabilises once the cell count exceeds approximately 1×10^5, remaining within a narrow band of 47.3–47.7 °C thereafter. The relative change in both the reference temperature and the thermal resistance R_{vc} between the selected mesh (M3, 102,181 cells) and the finest mesh (M6) is below 2%, which is considered acceptable for the present study. The 102,181-cell mesh is therefore adopted for all subsequent simulations to balance accuracy with computational efficiency.

3.8 Parametric Study Design

3.8.1 Case Setup

Once the baseline VC-16 case is established, a parametric study is conducted to investigate the influence of two design and operating variables: the number and arrangement of support ribs, and the imposed evaporator heat flux. All other settings (geometry envelope, mesh strategy, boundary conditions, numerical setup) remain identical to the baseline case described in Sections 3.2–3.5. Any deviation from the baseline is explicitly mentioned.

The full test matrix is summarised in Table 6.

The VC-N case is included primarily to confirm that the model captures the dryout behaviour expected from a structurally and thermally unsupported chamber, providing an indirect validation of the model in the absence of dedicated experimental data.

3.8.2 Output Parameters

The same output parameters as defined in Section 3.6 are extracted for each parametric case. For the comparison across heat flux levels, an additional emphasis is placed on the vapor volume fraction transient curve, which identifies whether the phase-change cycle has

Table 6: Test matrix for the parametric study.

Configuration	Rib count	Heat flux [kW/m^2]
VC-N	0	80
VC-12	12	80
VC-12	12	400
VC-12	12	800
VC-14	14	80
VC-14	14	400
VC-14	14	800
VC-16	16	80
VC-16	16	400
VC-16	16	800

been successfully initiated. Specifically, three operating regimes are distinguished based on the steady-state vapor volume fraction and pressure response:

- **Conduction-dominated regime**: VF remains below 0.01 and oscillates without reaching saturation; heat transfer is governed by solid and liquid conduction.
- **Fully phase-change regime**: VF reaches 1.0 within a few seconds and remains stable; the vapor chamber operates in its intended mode.
- **Near-critical regime**: VF saturates almost instantaneously, but evaporator-side temperatures exceed safe operating limits, indicating that the system is approaching the critical heat flux.

Convergence is determined by the stabilisation of the same key engineering parameters used in the baseline case.

4 Results

This chapter is dedicated to the presentation of the numerical results from the CFD simulations described in Chapter 3. The results are organised into two main sections: the verification of the CFD model through the no-rib baseline case, followed by an analysis of the influence of rib configuration and operating heat flux on the thermal-hydraulic performance of ultra-thin vapor chambers.

For all contour plots and flow fields presented, unless otherwise noted, the orientation of the quarter-domain is shown with the heat source at the bottom-centre and the condensation surface at the top. The four rib configurations investigated in this work are illustrated in Figure 6.

4.1 Model Verification through the No-Rib Baseline

This section provides detailed results from the VC-N baseline case, used to verify that the developed CFD model correctly captures the expected dryout behaviour of an unsupported ultra-thin vapor chamber.

4.1.1 Transient Behaviour of the VC-N Configuration

Figure 10 presents the transient evolution of the maximum wick (wall) temperature and the average vapor-core temperature for the VC-N configuration at 80 kW/m^2. Starting from the initial ambient value of 26.85 °C, the wick temperature rises monotonically—with a brief inflection near 5 s—and stabilises at approximately 197 °C after about 30 s. Over the same period the average vapor-core temperature does not rise at all: it stays at, and briefly slightly below, its initial value, never thermally activating.

The brief excursion of the average vapor-core temperature a few kelvin below its initial value during the first seconds of the simulation (Figure 10) is a numerical start-up transient and carries no physical significance. It arises from the coupled initialisation of the compressible (ideal-gas) vapor field at the operating pressure together with the stiff Lee phase-change source terms, which can transiently over- or under-shoot the local energy balance in the near-empty vapor cells before the field settles. It does not represent physical sub-cooling, flash evaporation, or freezing of the working fluid: the saturation temperature is held fixed at T_{sat} = 50 °C throughout (Section 3.3), so no genuine low-temperature phase state exists in the model. The transient decays within the first few time steps and does not affect the steady-state conclusion that the wick overheats to roughly 197 °C while the vapor core never thermally activates.

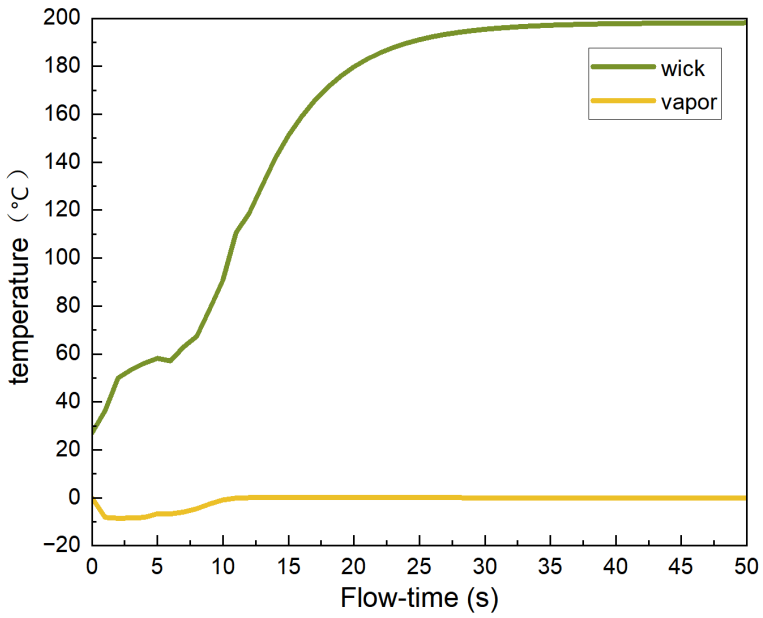


Figure 10: Transient evolution of the maximum wick (wall) temperature and the average vapor-core temperature for the VC-N configuration at 80 kW/m^2. The wick temperature stabilises near 197 °C after about 30 s, while the vapor-core temperature never rises above its initial value, indicating that the two-phase cycle is never established.

The steady-state temperature field is shown in Figure 11: the peak temperature is concentrated over the centred heat source and decays laterally towards the cooled edges, the signature of in-plane conduction through the solid envelope and wick rather than heat transport through the vapor core. The chamber therefore reaches a steady state, but a degenerate one. Without the ribs to bleed heat across the core and to return condensate,

the heat input concentrates at the evaporator: the wick superheats to ≈197 °C and boils off the local liquid inventory, so the vapor volume fraction climbs toward unity (Figure 12). This saturation is, however, a symptom of boil-off rather than of healthy operation—the vapor neither circulates nor releases its latent heat at the condenser, the average vapor-core temperature never rises (Figure 10), and the evaporation–condensation cycle is never established.

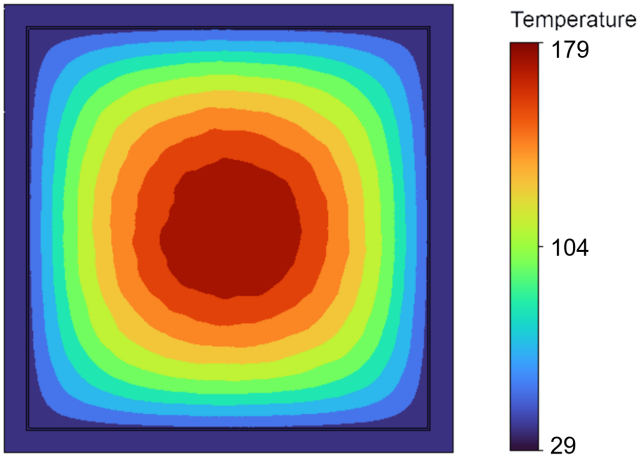


Figure 11: Steady-state temperature contour of the VC-N configuration at 80 kW/m^2. The peak temperature (≈179 °C in the plane shown) is concentrated over the heat source and spreads laterally to the cooled edges, while the vapor core remains thermally inactive—confirming the absence of a functioning evaporation–condensation cycle. The ≈179 °C peak is read on the displayed plane and is therefore lower than the 197 °C maximum wick temperature reported in Figure 10.

By comparison, the supported VC-12 settles at a wick temperature of about 164 °C *with an active vapor core at 145 °C*. The VC-N case is thus both hotter and, more importantly, entirely lacking a *closed*, working vapor cycle. This behaviour is consistent with the dual mechanical-and-capillary role of support structures highlighted by Jiang et al. [19], and reverse-validates the indispensability of the support ribs for establishing an active phase-change cycle in ultra-thin vapor chamber operation.

4.2 Influence of Rib Configuration

This section compares the steady-state behaviour of the three supported configurations (VC-12, VC-14, VC-16) at the medium heat flux of 400 kW/m^2 to isolate the effect of rib number and arrangement. (The no-rib VC-N case was simulated only at 80 kW/m^2 and is treated separately as the verification case in Section 4.1.) The comparison is interpreted not only through the resulting temperatures but also through the vapor volume fraction (VF), which determines whether each configuration is actually operating as a phase-change device at this heat flux.

As a consolidated view of the operating-regime behaviour discussed above, Figure 12 compares the transient evolution of the vapor volume fraction (VF) for the four configurations (VC-N only at 80 kW/m^2). Two points are worth emphasising. First, the unsupported VC-N chamber, simulated only at 80 kW/m^2, never establishes a *closed* two-phase cycle. Its vapor volume fraction does rise toward unity, but only because the superheated evaporator

boils off the local liquid; with no rib-assisted condensate return the loop never closes, the vapor stays stagnant, and the wall runs away to ≈197 °C (Figures 10 and 11). This boil-off saturation must be read together with the runaway wall temperature and the absence of vapor circulation—together they confirm dryout, not healthy operation, and that an unsupported ultra-thin chamber cannot sustain two-phase operation and that the support ribs are indispensable for activating the phase-change cycle. Second, among the supported layouts the figure makes the central inverse coupling visually explicit: at 80 kW/m^2 none of VC-12, VC-14 or VC-16 establishes a vapor phase, whereas at the higher fluxes the onset of phase change is progressively delayed and weakened as the rib count grows. VC-12 saturates within about 2–3 s at both 400 and 800 kW/m^2; VC-14 reaches only partial saturation (≈ 0.88) at 400 kW/m^2 and full saturation at 800 kW/m^2; and VC-16 fails to activate at 400 kW/m^2 and only slowly climbs towards ≈ 0.87 over nearly 30 s at 800 kW/m^2. The lengthening of the saturation time with rib density—from a few seconds for VC-12 to tens of seconds for VC-16—is itself a signature of the shift from latent-heat transport towards solid conduction.

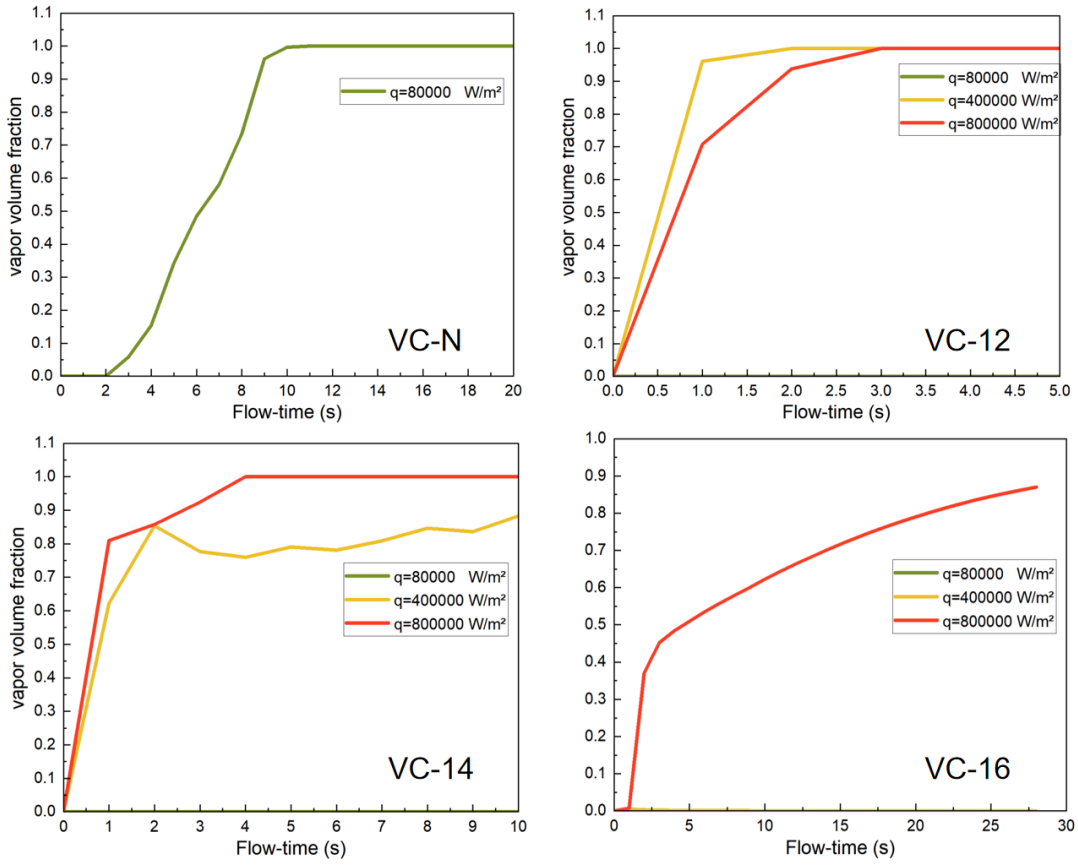


Figure 12: Transient evolution of the vapor volume fraction (VF): VC-N at 80 kW/m^2 only, and VC-12, VC-14 and VC-16 at 80, 400 and 800 kW/m^2. The unsupported VC-N chamber dries out at 80 kW/m^2: its VF climbs toward unity as the superheated evaporator boils off the liquid, but with no rib-assisted condensate return the cycle never closes (cf. the runaway wall temperature in Figure 10), so this saturation reflects boil-off rather than active two-phase operation. Among the supported layouts the onset of phase change is progressively delayed and weakened as the rib count increases, illustrating the inverse coupling between rib density and active two-phase operation.

4.2.1 Steady-State Performance Comparison

Table 7 summarises the steady-state indicators of the configurations at 400 kW/m^2. The peak wick, ribs and vapor temperatures, the steady-state vapor volume fraction, and the vapor-core pressure drop are extracted directly from the transient monitors and field exports.

Table 7: Steady-state comparison of the three supported configurations at 400 kW/m^2. (The no-rib VC-N case was simulated only at 80 kW/m^2; see Section 4.1.)

Config	$T_{\text{wick,max}}$ [°C]	T_{vapor} [°C]	VF	ΔP_{vc} [Pa]	Regime
VC-12	163.8	145.0	1.0	0.059	Fully phase-change
VC-14	94.4	73.8	0.88	1.82	Partial phase-change
VC-16	44.8	42.0	≈0.005	8.6×10^{-5}	Conduction-dominated

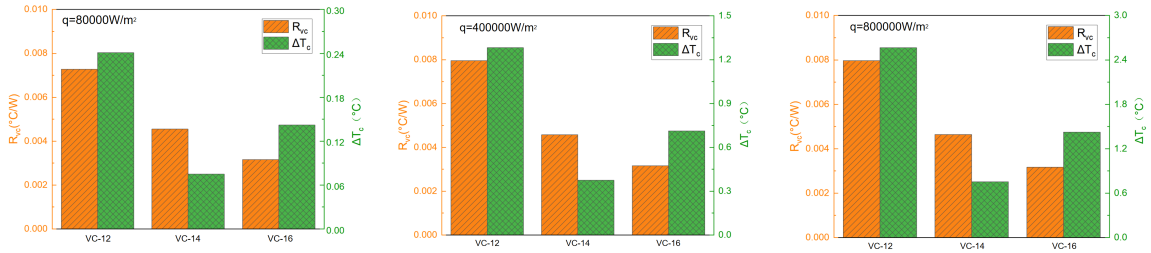
Two trends emerge, and they run in opposite directions. First, the peak wick temperature falls monotonically as the rib count increases, from 163.8 °C for VC-12 to 94.4 °C for VC-14 and 44.8 °C for VC-16. Taken in isolation, this would suggest that a denser rib array is thermally superior. Second, however, the steady-state vapor volume fraction falls in the *same* direction: VC-12 reaches full saturation (VF = 1.0), VC-14 only attains partial saturation (VF ≈ 0.88), and VC-16 never establishes a vapor phase at all (VF ≈ 0.005). The denser the rib array, the less the chamber behaves as a vapor chamber at this heat flux.

This inverse coupling is the central result of the comparison: the low peak temperature of VC-16 is *not* evidence of superior two-phase performance, but a consequence of the chamber operating in a conduction-dominated regime. With the largest number of porous copper ribs spanning the vapor core, VC-16 presents so many parallel solid-conduction paths between the evaporator and condenser walls that heat is removed by conduction before the wick can reach the conditions required to sustain evaporation. At 400 kW/m^2 it therefore behaves essentially as a near-solid metallic spreader rather than as an active vapor chamber. Conversely, VC-12, with its wider central vapor channel, is the only one of the three operating in its intended fully-developed phase-change mode at this heat flux, which is also why it exhibits the highest evaporator-side temperature: the latent-heat transport is active but the device is loaded close to its working point.

Figure 13 presents the two performance indicators defined in Section 2.3 for the three configurations across the three heat-flux levels: the overall thermal resistance R_{vc}, which quantifies the total opposition to heat flow from the evaporator to the condenser and therefore reflects the global heat-spreading capability, and the condenser-surface temperature non-uniformity $\Delta T_c = T_{c,\max} - T_{c,\min}$, which measures the severity of local hotspots on the condenser side. A lower R_{vc} indicates more efficient heat spreading, while a smaller ΔT_c indicates a more uniform condenser surface; the two are reported together because, as shown below, they do not necessarily favour the same rib configuration.

4.2.2 Wall Temperature Distribution

Figure 14 compares the steady-state wall temperature contours of the three configurations across the three heat-flux levels. At 400 kW/m^2, the VC-12 configuration exhibits a pronounced "X"-shaped pattern of elevated temperature concentrated over the heat source and in the gaps between adjacent ribs, with a peak temperature of approximately 164 °C.



(a) $q'' = 80$ kW/m^2 **(b)** $q'' = 400$ kW/m^2 **(c)** $q'' = 800$ kW/m^2

Figure 13: Overall thermal resistance R_{vc} and condenser-surface temperature non-uniformity ΔT_c for the three rib configurations at 80, 400 and 800 kW/m^2.

This is the signature of an active evaporator with localised hot zones between the conduction paths. As ribs are added (VC-14, then VC-16), the field becomes progressively flatter and cooler, with VC-16 showing the most uniform distribution and the lowest peak. However, this flattening reflects the suppression of the localised evaporation hot spots by solid conduction rather than an improvement in vapor spreading.

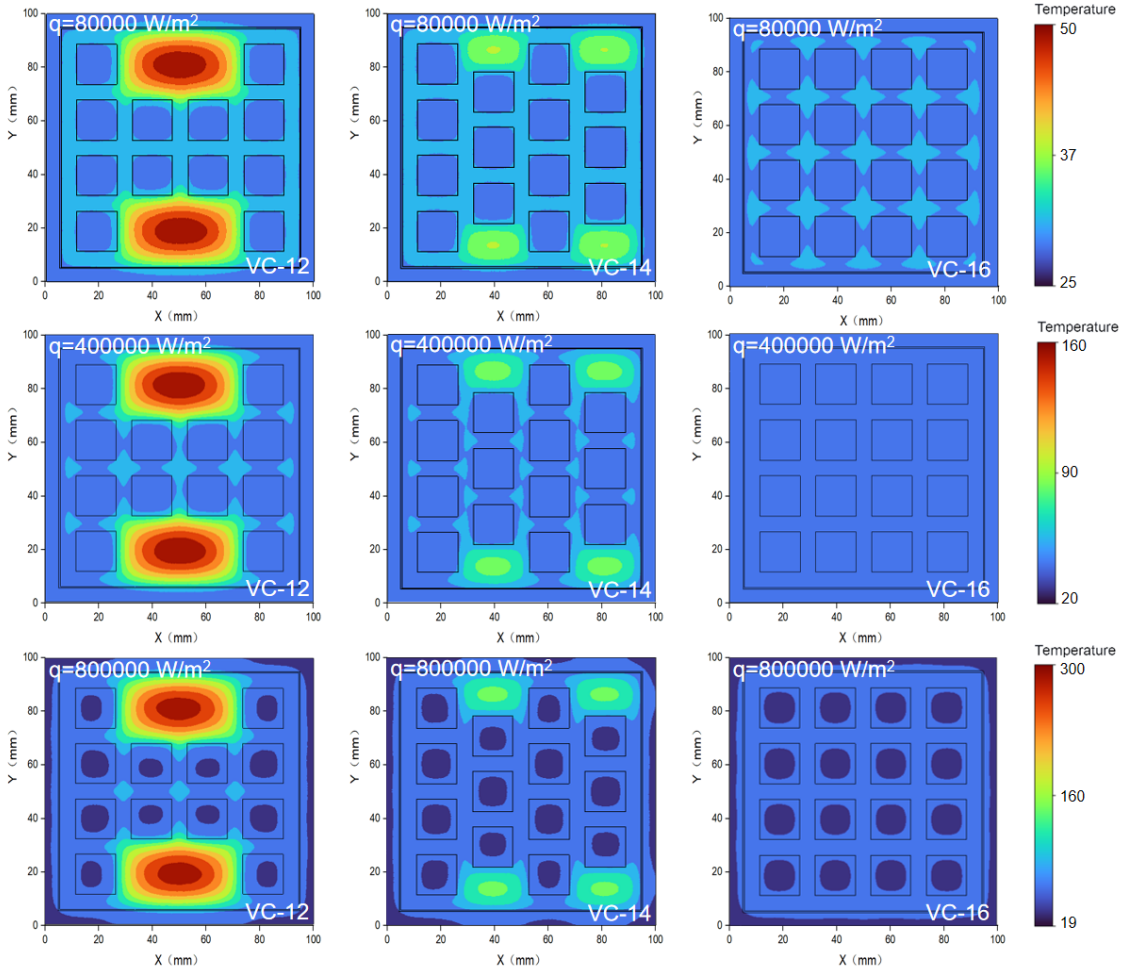
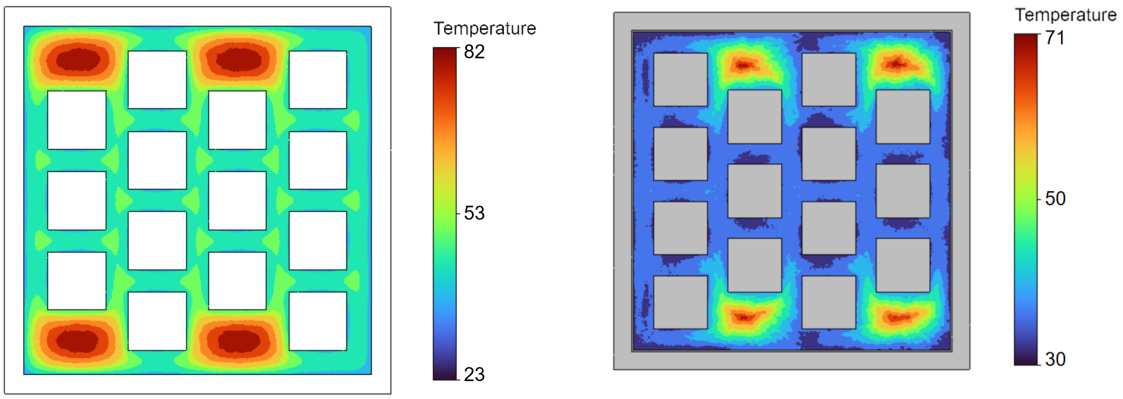


Figure 14: Steady-state wall temperature contours of VC-12, VC-14 and VC-16 (columns) at 80, 400 and 800 kW/m^2 (rows), each row under a common colour scale.

This reframes the comparison with the reference study. Jiang et al. [19] observed that

support columns act as preferential heat-conduction paths and that a denser column array lowers the apparent thermal resistance and yields a more uniform wall. The present results reproduce the same temperature ordering, but make explicit the mechanism behind it: within the tested geometry, increasing the rib count shifts the chamber from phase-change-dominated operation (VC-12) towards conduction-dominated operation (VC-16). The lower peak temperature is thus obtained at the cost of disabling the phase-change cycle, the very mechanism a vapor chamber is designed to exploit.

The wick and vapor core temperature distributions for the VC-14 case at 400 kW/m^2 are presented in Figure 15 for completeness.



(a) Wick **(b)** Vapor core

Figure 15: Steady-state wick and vapor core temperature contours for the VC-14 configuration at 400 kW/m^2.

4.2.3 Vapor Flow Field Characteristics

The vapor velocity field around the support ribs is shown in Figure 16 for all three configurations across the three heat-flux levels. Wherever an active vapor phase is present, the flow exhibits the typical bluff-body pattern around the ribs: streamline deflection at the leading edge, acceleration along the sides, and separation at the trailing edge. The separated shear layers enclose a low-velocity recirculation region immediately behind each rib—a wake dead zone in which the vapor is largely stagnant and contributes little to the net throughflow. These dead zones are a parasitic effect of the support structure: they occupy part of the vapor core without participating in latent-heat transport, and they grow more pronounced as the rib array becomes denser and the inter-rib channels narrower. The features are most clearly developed in the cases that actually sustain phase change (VC-12 at the medium and high flux levels, and VC-14 and VC-16 at 800 kW/m^2).

Because each subplot in Figure 16 carries its own velocity colour scale, the absolute vapor speeds cannot be compared directly across cases from the colours alone; the comparison is therefore anchored by the vapor volume fraction and the vapor-core pressure drop reported in Table 7. For VC-16 at 400 kW/m^2, the near-zero vapor volume fraction (VF $\approx$ 0.005) means there is negligible vapor throughflow, and the velocity field is correspondingly weak; here the entire core is effectively stagnant rather than exhibiting localised wake dead zones, so the very small pressure drop reported for this case ($\sim$8.6 $\times$ 10^{-5} Pa) reflects a near-stagnant vapor core rather than an efficiently flowing one. The wider channels of

VC-12 sustain a genuine vapor circulation at lower flow resistance, whereas the dense VC-16 array both constrains the channel—enlarging the inter-rib wake dead zones where an active vapor phase does exist—and, at the design flux, largely removes the driving phase change altogether.

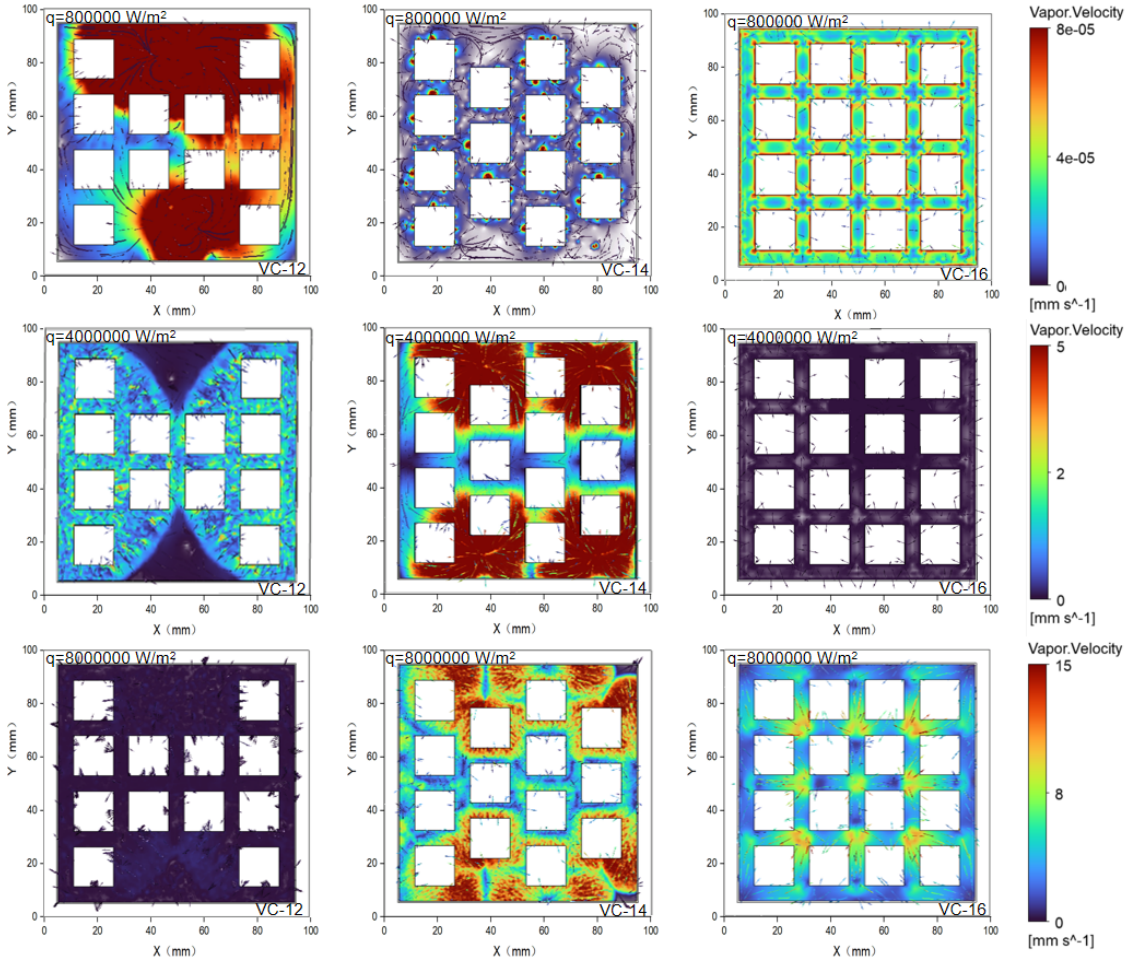


Figure 16: Steady-state vapor velocity vectors and streamlines for VC-12, VC-14 and VC-16 (columns) across the three heat-flux levels (rows), showing bluff-body wake patterns around the ribs. Note that each subplot uses its own velocity colour scale (see the individual colour bars), so the colours indicate the flow pattern within each case and must not be read as an absolute velocity comparison across subplots; the magnitude of the vapor throughflow is instead quantified by the vapor volume fraction and the vapor-core pressure drop reported in Table 7.

Because each subplot in Figure 16 carries its own velocity colour scale, the absolute vapor speeds cannot be compared directly across cases from the colours alone; the comparison is therefore anchored by the vapor volume fraction (Table 7).

For VC-16 at 400 kW/m^2, by contrast, the near-zero vapor volume fraction means there is negligible vapor throughflow, and the velocity field is correspondingly weak; the very small pressure drop reported for this case ($\sim 8.6 \times 10^{-5}$ Pa) reflects this near-stagnant vapor core rather than an efficiently flowing one. The wider channels of VC-12 sustain a genuine vapor circulation at lower flow resistance, whereas the dense VC-16 array both constrains the channel and, at the design flux, largely removes the driving phase change altogether.

4.3 Detailed Per-Configuration Analysis

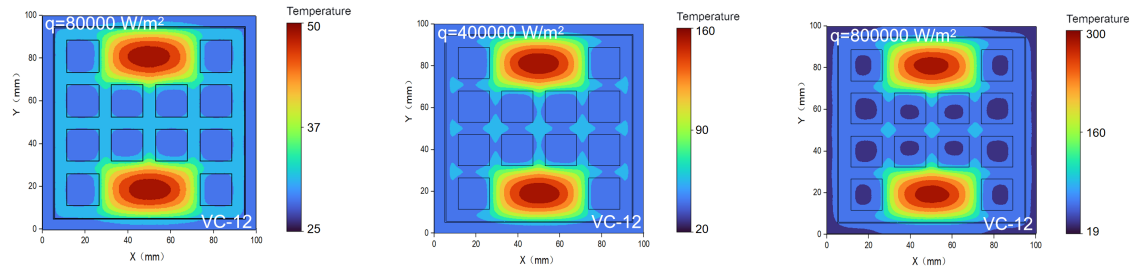
Whereas Section 4.2 established the central inverse-coupling mechanism through a direct cross-configuration comparison, this section serves a different purpose: it documents the complete set of field results for each configuration across all three heat-flux levels, providing the per-design evidence that underpins the comparative conclusions already drawn. The discussion here is therefore deliberately descriptive rather than interpretive, and readers seeking the main mechanism should refer to Section 4.2.

Each configuration is now examined field by field across the three heat-flux levels, following the per-design presentation of Jiang et al. [19]. For every configuration the following are reported: the condenser wall-temperature contour, the wick and vapor-core temperature contours, the diagonal cross-section temperature, the vapor-velocity field, the vapor-core pressure distribution, and the transient temperature and vapor-volume-fraction curves, together with the $R_{vc}/\Delta T_c$ response to heat flux.

4.3.1 VC-12 (wide central channel)

VC-12 is developed vapor chamber across the whole tested range. Its wall-temperature contour (Figure 17) retains the "X"-shaped hot zone at every heat flux, intensifying from 80 to 800 kW/m^2. The wick and vapor-core temperature fields (Figures 18 and 19) show the latent-heat exchange concentrated over the heat source, and the diagonal section (Figure 20) confirms a steep evaporator-side gradient that relaxes towards the condenser. The vapor-velocity field (Figure 21) develops a genuine circulation through the wide central channel, and the pressure field (Figure 22) remains extremely flat (~2.5, 0.06 and 0.001 Pa at 80, 400 and 800 kW/m^2), confirming that vapor-flow resistance is never the limiting factor.

The transient curves identify three regimes (Figure 23): at 80 kW/m^2 the vapor fraction oscillates near zero (conduction-dominated); at 400 kW/m^2 it saturates within ~3 s with a moderate wick–vapor gap of ~19 K (optimal regime); at 800 kW/m^2 it saturates almost instantly but the wick exceeds 300 °C (near-critical). The $R_{vc}/\Delta T_c$ response (Figure 24) shows ΔT_c rising steeply with heat flux while R_{vc} stays low, consistent with a device loaded towards its working point.

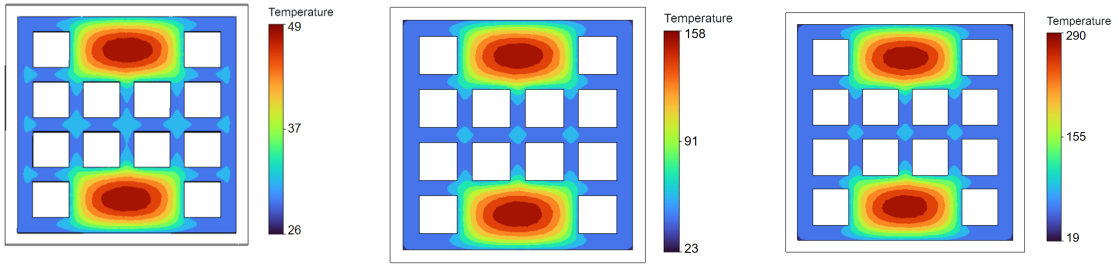


(a) 80 kW/m^2 **(b)** 400 kW/m^2 **(c)** 800 kW/m^2

Figure 17: VC-12 condenser wall-temperature contours at the three heat-flux levels.

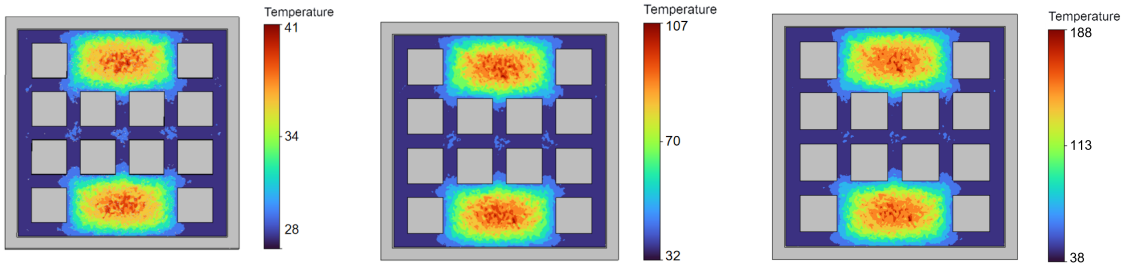
4.3.2 VC-14 (intermediate)

VC-14 represents the transition between regimes. The wall-temperature contour (Figure 25) is markedly flatter than VC-12, with residual hot bands near the open rows. The wick



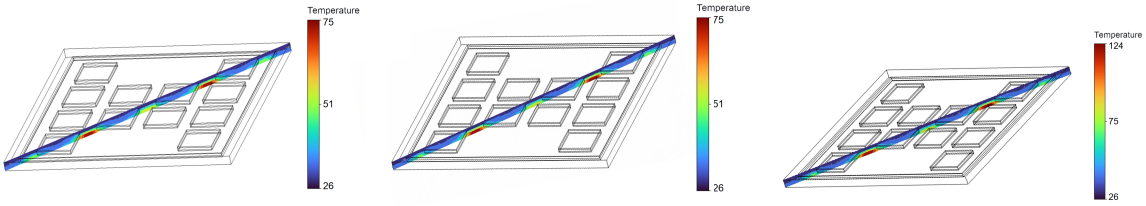
(a) 80 kW/m^2 **(b)** 400 kW/m^2 **(c)** 800 kW/m^2

Figure 18: VC-12 wick-temperature contours at the three heat-flux levels.



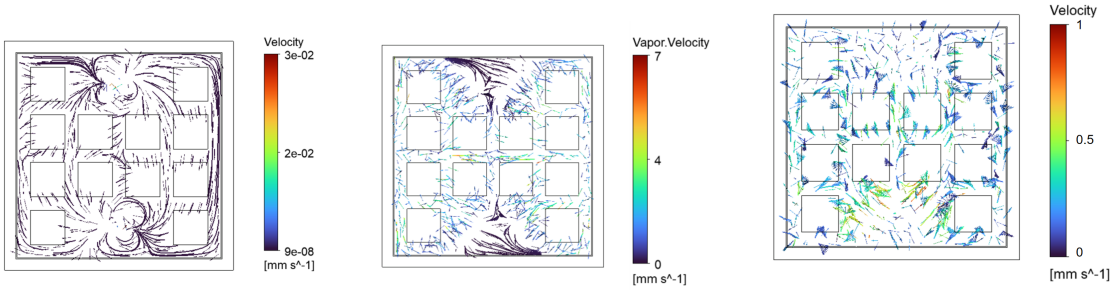
(a) 80 kW/m^2 **(b)** 400 kW/m^2 **(c)** 800 kW/m^2

Figure 19: VC-12 vapor-core temperature contours at the three heat-flux levels.



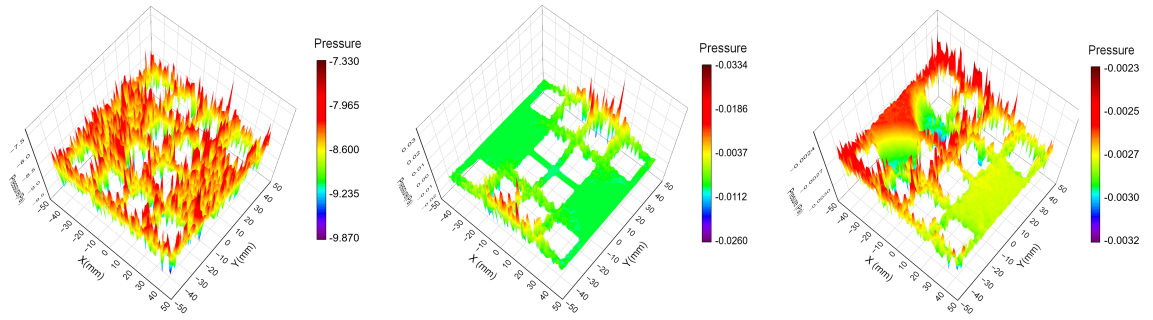
(a) 80 kW/m^2 **(b)** 400 kW/m^2 **(c)** 800 kW/m^2

Figure 20: VC-12 diagonal cross-section temperature contours at the three heat-flux levels.



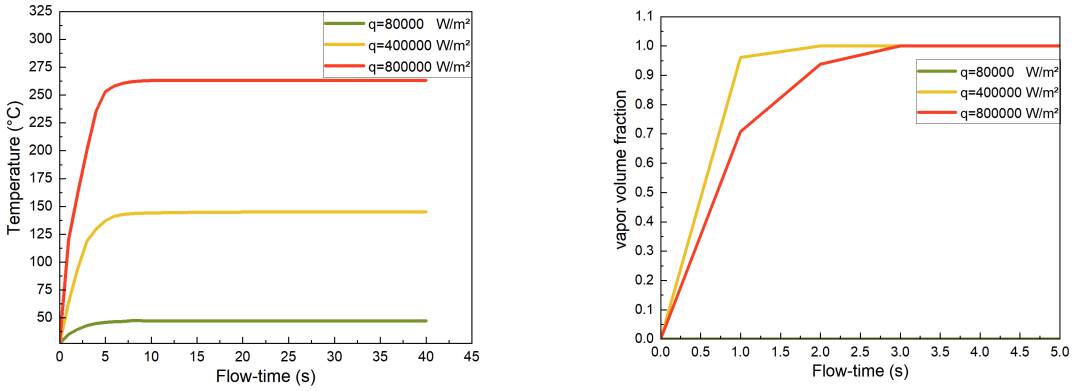
(a) 80 kW/m^2 **(b)** 400 kW/m^2 **(c)** 800 kW/m^2

Figure 21: VC-12 vapor-velocity vector fields at the three heat-flux levels.



(a) 80 kW/m^2 **(b)** 400 kW/m^2 **(c)** 800 kW/m^2

Figure 22: VC-12 steady-state vapor-core pressure distributions at the three heat-flux levels. Because the vapor-flow resistance in the wide central channel is very low, the absolute pressure variation is small (on the order of a few pascal at most), so each colour scale spans only a narrow range; the apparent surface texture therefore reflects the very flat pressure field rather than a strong physical gradient.



(a) Transient temperature **(b)** Vapor volume fraction

Figure 23: VC-12 transient response at 80, 400 and 800 kW/m^2: (a) maximum wall/wick/vapor temperature; (b) vapor volume fraction.

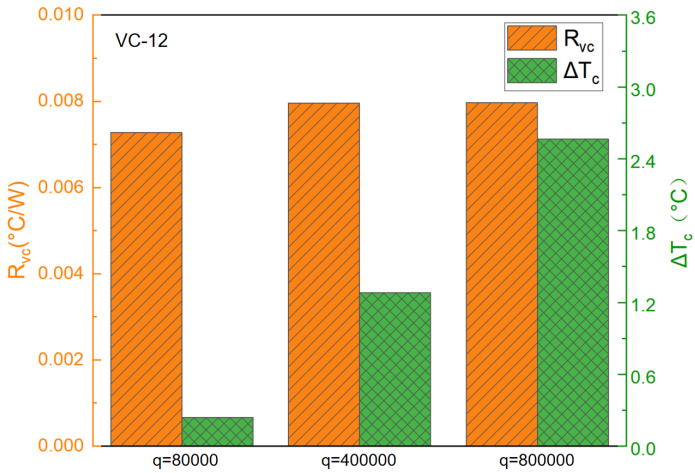
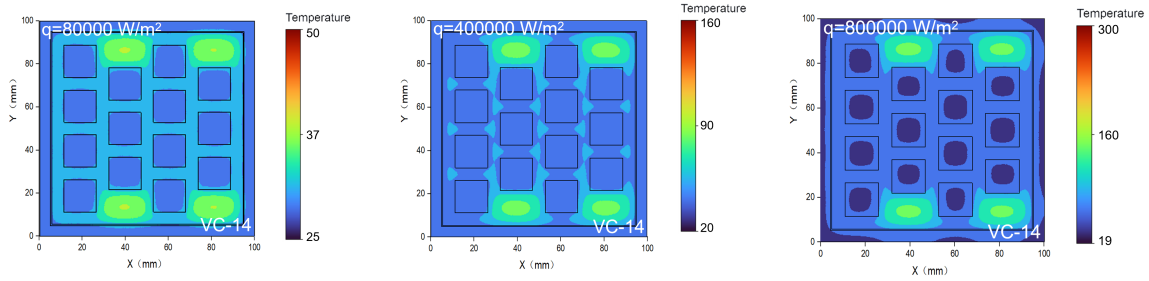


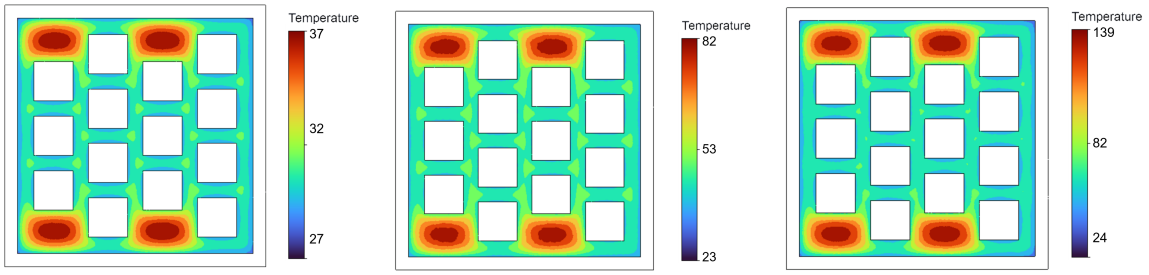
Figure 24: VC-12: thermal resistance R_{vc} and condenser temperature non-uniformity ΔT_c as a function of heat flux.

and vapor-core temperature fields (Figures 26 and 27) show partial latent-heat activity, and the diagonal section (Figure 28) a reduced evaporator gradient. The vapor-velocity field (Figure 29) sustains bluff-body wakes only once phase change is active (most clearly at 800 kW/m^2), and the pressure field (Figure 30) remains low. The transient curves (Figures 31 and 32) show the vapor fraction stabilising near 0.88 at 400 kW/m^2 (partial saturation) and reaching unity only at 800 kW/m^2. The $R_{vc}/\Delta T_c$ response (Figure 33) gives the lowest ΔT_c of the three configurations at 400 kW/m^2.



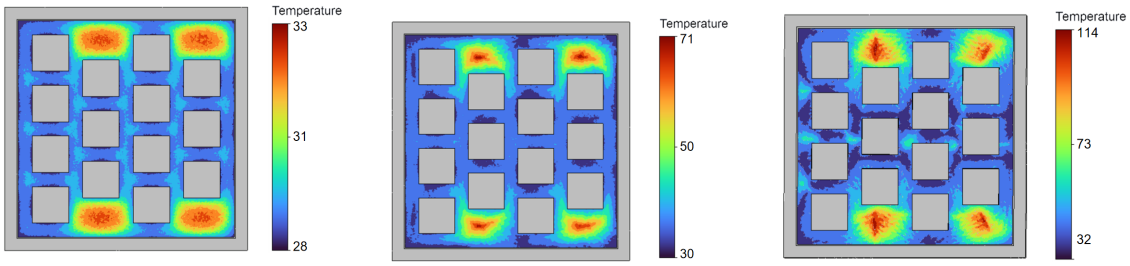
(a) 80 kW/m^2 **(b)** 400 kW/m^2 **(c)** 800 kW/m^2

Figure 25: VC-14 condenser wall-temperature contours at the three heat-flux levels.



(a) 80 kW/m^2 **(b)** 400 kW/m^2 **(c)** 800 kW/m^2

Figure 26: VC-14 wick-temperature contours at the three heat-flux levels.

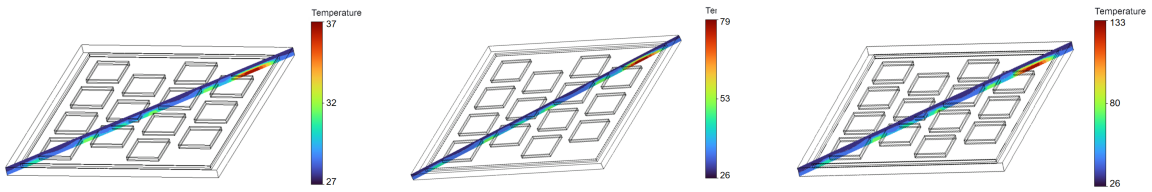


(a) 80 kW/m^2 **(b)** 400 kW/m^2 **(c)** 800 kW/m^2

Figure 27: VC-14 vapor-core temperature contours at the three heat-flux levels.

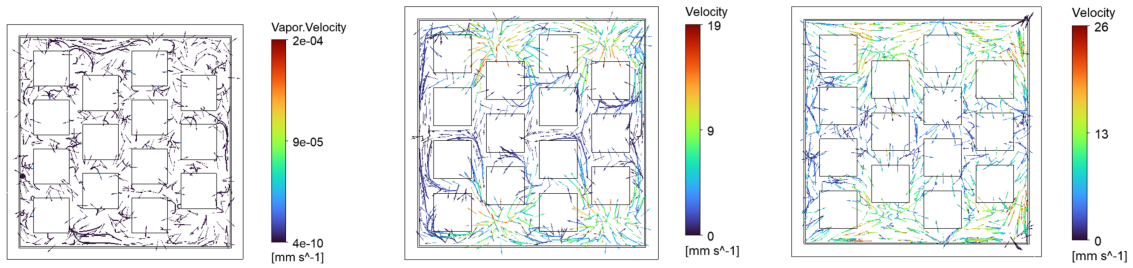
4.3.3 VC-16 (dense 4×4 matrix)

VC-16 gives the lowest peak temperature but, at the design flux, the lowest two-phase activity. The wall-temperature contour (Figure 34) is nearly flat — a near-solid metallic



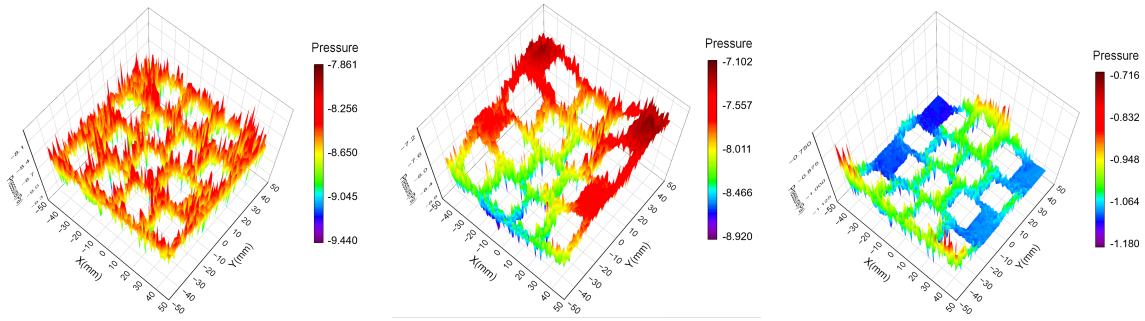
(a) 80 kW/m^2 **(b)** 400 kW/m^2 **(c)** 800 kW/m^2

Figure 28: VC-14 diagonal cross-section temperature contours at the three heat-flux levels.



(a) 80 kW/m^2 **(b)** 400 kW/m^2 **(c)** 800 kW/m^2

Figure 29: VC-14 vapor-velocity vector fields at the three heat-flux levels.



(a) 80 kW/m^2 **(b)** 400 kW/m^2 **(c)** 800 kW/m^2

Figure 30: VC-14 steady-state vapor-core pressure distributions at the three heat-flux levels. At 80 kW/m^2 the chamber is conduction-dominated and the core is near-stagnant, so the pressure field shows only negligible, noise-level variation; at 400 and 800 kW/m^2 a partial-to-full phase-change cycle develops and the pressure field becomes physically meaningful, though the absolute drop remains small.

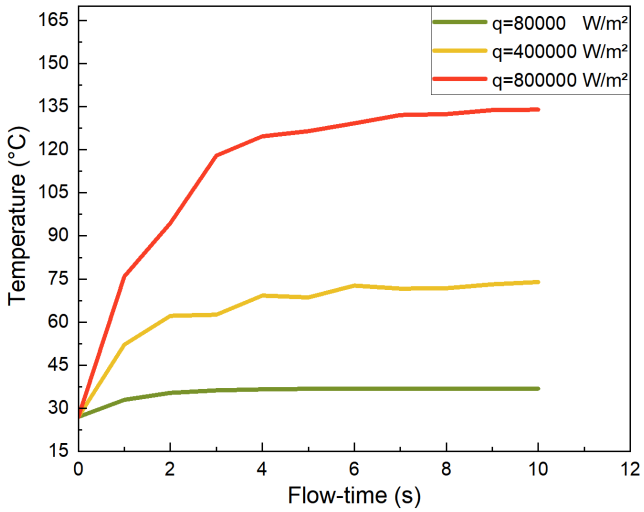


Figure 31: VC-14 transient maximum wall/wick/vapor temperature at 80, 400 and 800 kW/m^2.

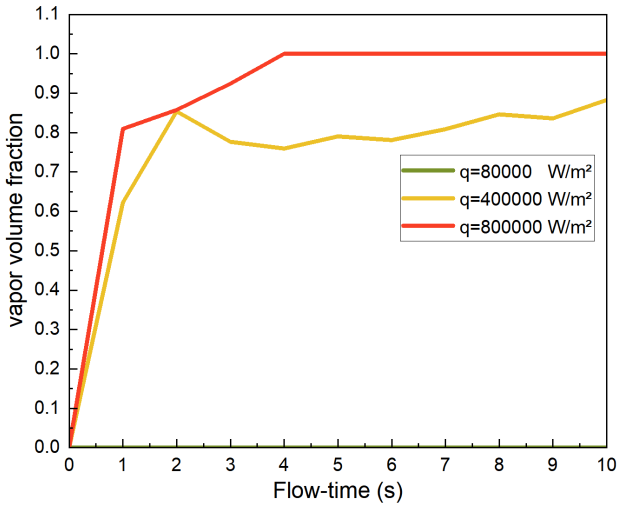


Figure 32: VC-14 transient vapor volume fraction at 80, 400 and 800 kW/m^2.

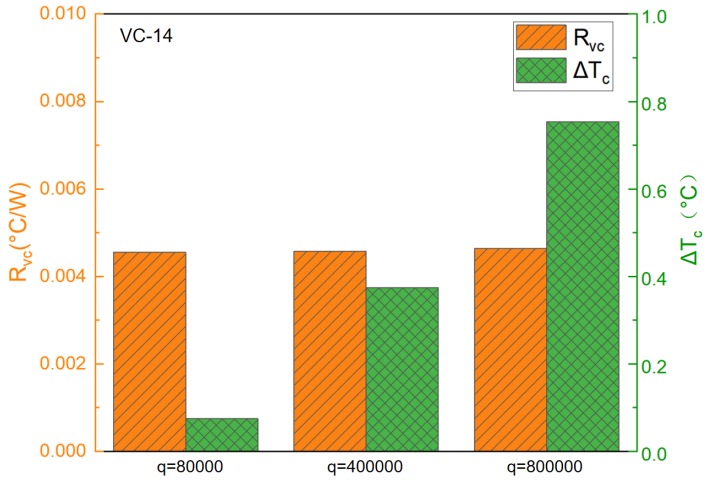
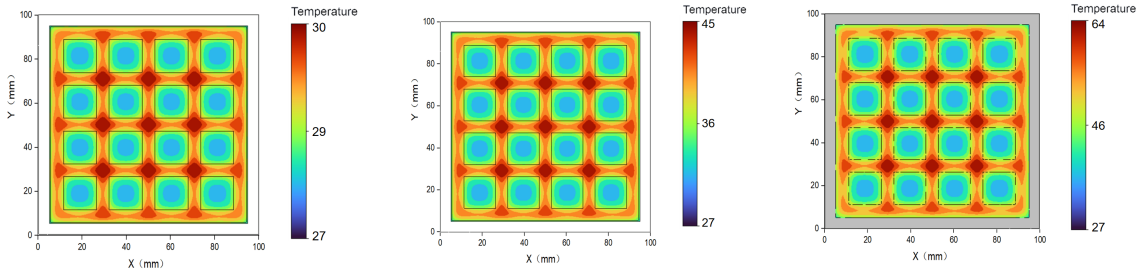


Figure 33: VC-14: thermal resistance R_{vc} and condenser temperature non-uniformity ΔT_c as a function of heat flux.

spreader rather than an active vapor chamber at 400 kW/m^2. The diagonal section (Figure 36) shows an almost linear conduction profile. For the velocity field, both the vector representation (Figure 37) and the magnitude contour (Figure 38) are given(The vector field (Figure 37) is presented as a top view of the whole vapor core, whereas the magnitude contour (Figure 38) is taken on a mid-plane slice; the two therefore use different colour scales and are not intended for direct one-to-one comparison.): at 80 and 400 kW/m^2 the vapor throughflow is negligible (peak $\sim 10^{-5}$ mm/s), and only at 800 kW/m^2 does a genuine vapor circulation develop. The pressure field (Figure 39) is correspondingly near-stagnant. The transient curves (Figures 40 and 41) confirm that the vapor fraction never saturates at 400 kW/m^2 and only slowly rises at 800 kW/m^2, while the $R_{vc}/\Delta T_c$ response (Figure 42) gives the lowest R_{vc} overall — a value that nonetheless reflects near-solid conduction rather than efficient two-phase operation, since the vapor phase is essentially absent at this heat flux.



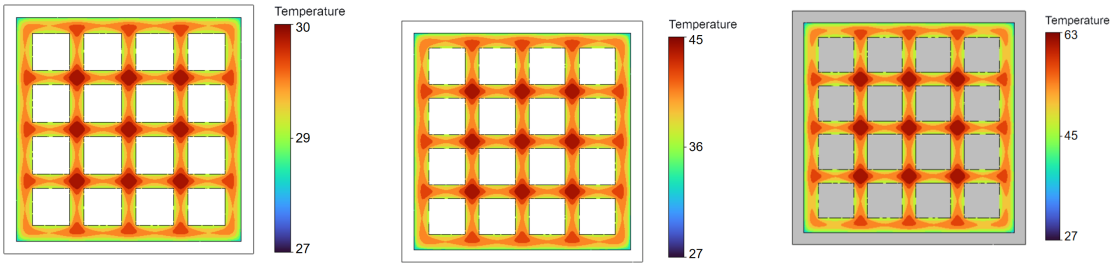
(a) 80 kW/m^2 **(b)** 400 kW/m^2 **(c)** 800 kW/m^2

Figure 34: VC-16 condenser wall-temperature contours at the three heat-flux levels.

4.4 Summary of Key Findings

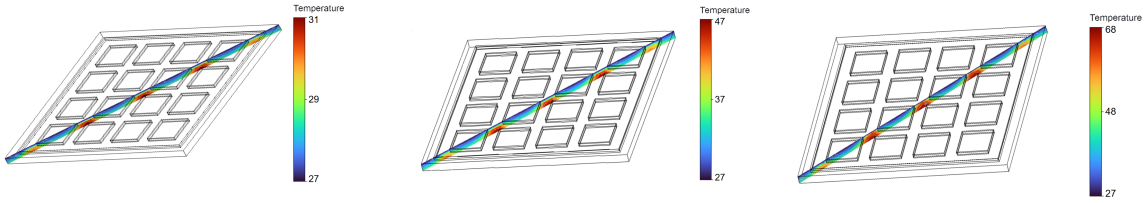
Based on the analyses above, the following key observations can be drawn:

1. Without support ribs, the vapor chamber fails to establish an active two-phase cycle:



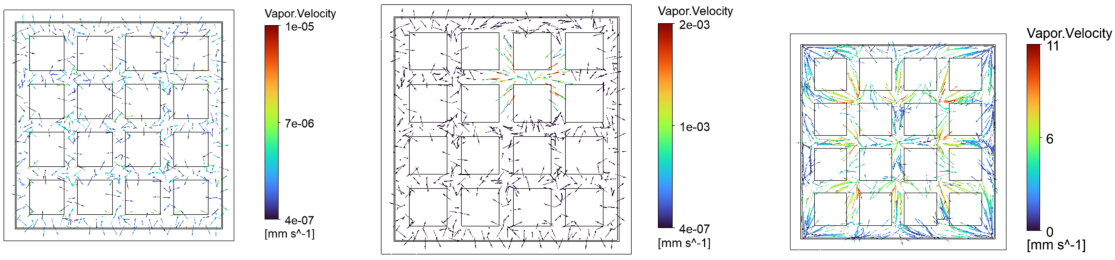
(a) 80 kW/m^2 **(b)** 400 kW/m^2 **(c)** 800 kW/m^2

Figure 35: VC-16 wick-temperature contours at the three heat-flux levels. The near-uniform field reflects conduction-dominated operation; the vapor core remains essentially inactive and is therefore not shown separately.



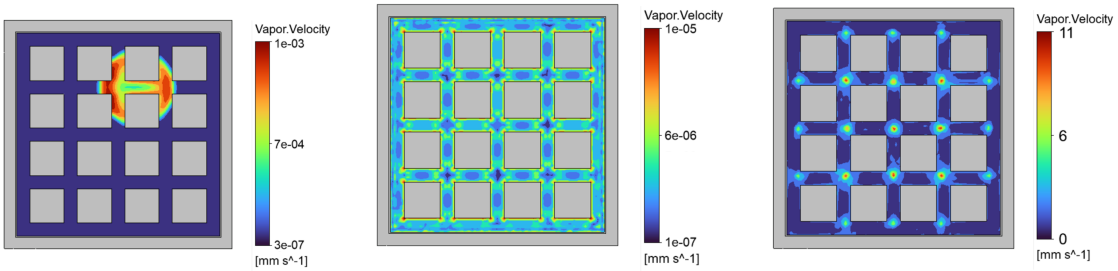
(a) 80 kW/m^2 **(b)** 400 kW/m^2 **(c)** 800 kW/m^2

Figure 36: VC-16 diagonal cross-section temperature contours at the three heat-flux levels.



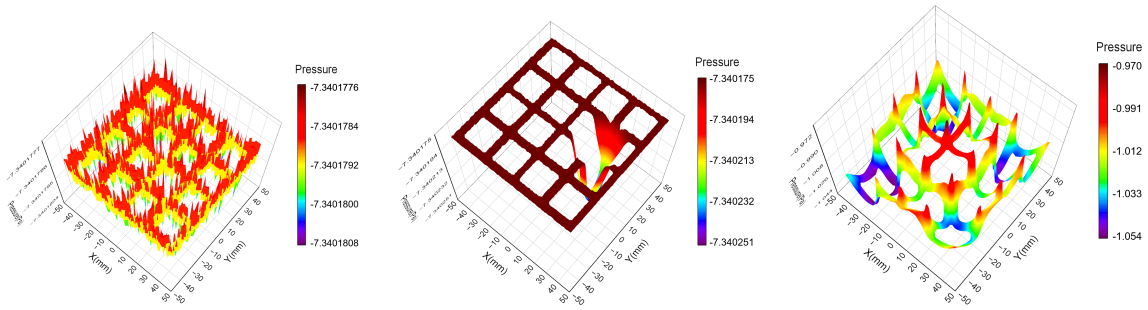
(a) 80 kW/m^2 **(b)** 400 kW/m^2 **(c)** 800 kW/m^2

Figure 37: VC-16 vapor-velocity vector fields at the three heat-flux levels, shown as a top (plan) view of the entire vapor core. Note that the colour scale differs from that of the mid-plane slice in Figure 38, as the two figures sample different regions of the vapor core.



(a) 80 kW/m^2 **(b)** 400 kW/m^2 **(c)** 800 kW/m^2

Figure 38: VC-16 vapor-velocity magnitude contours at the three heat-flux levels, extracted on a horizontal mid-plane slice through the vapor core (rather than the full-volume top view of Figure 37). Because the two figures are sampled on different planes, their colour-scale ranges are not directly comparable. At 80 and 400 kW/m^2 the throughflow is negligible (peak velocities on the order of 10^{-5} mm/s), consistent with the conduction-dominated state; only at 800 kW/m^2 does a genuine vapor circulation develop.



(a) 80 kW/m^2 **(b)** 400 kW/m^2 **(c)** 800 kW/m^2

Figure 39: VC-16 steady-state vapor-core pressure distributions at the three heat-flux levels. The pressure variation across the near-stagnant core is extremely small (of the order of 10^{-5} Pa about a mean of ~7.34 Pa), so the colour scale resolves only numerical noise rather than a physically meaningful pressure gradient; this is consistent with the conduction-dominated, near-zero-throughflow state of VC-16 at this heat flux.

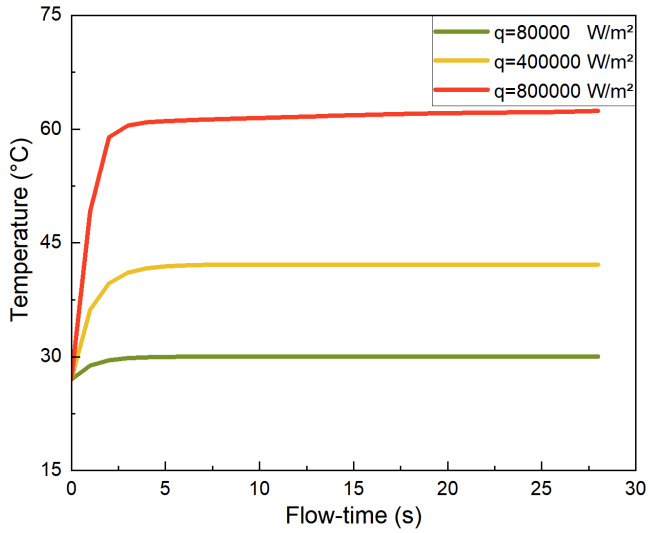


Figure 40: VC-16 transient maximum wall/wick/vapor temperature at 80, 400 and 800 kW/m^2.

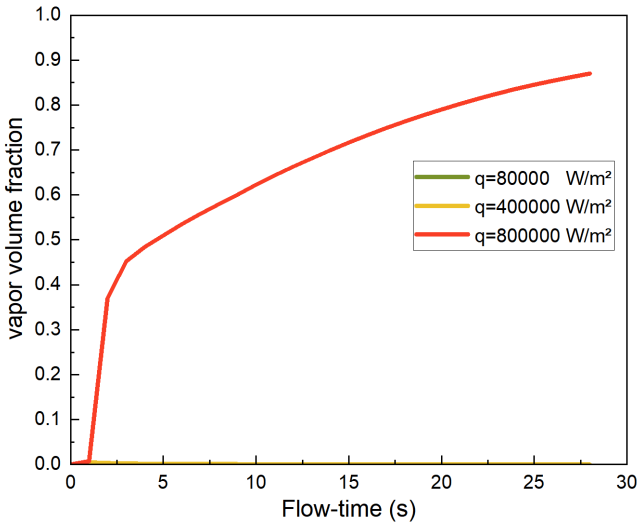


Figure 41: VC-16 transient vapor volume fraction at 80, 400 and 800 kW/m^2.

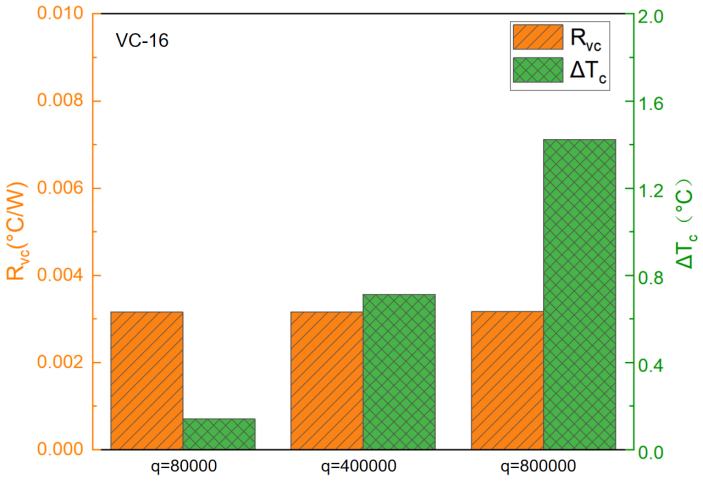


Figure 42: VC-16: thermal resistance R_{vc} and condenser temperature non-uniformity ΔT_c as a function of heat flux.

the VC-N case reaches a degenerate, conduction-only steady state in which the evaporator wick overheats to approximately 197 °C and boils off the local liquid (vapor volume fraction rising toward unity), yet the vapor never circulates or condenses back, so the vapor core stays thermally inactive and the two-phase cycle is never established. This validates the indispensability of support ribs as combined mechanical–capillary structures.

2. The two performance indicators do not order the three configurations identically at 400 kW/m²; each is therefore discussed separately below:

   - **Thermal resistance R_{vc} decreases monotonically with rib count**: $R_{vc} \approx 0.0080$ °C/W for VC-12, 0.0046 for VC-14, and 0.0032 for VC-16 (Figure 13). The densest VC-16 array therefore gives the lowest R_{vc}, because its larger number of porous-copper ribs adds the most parallel conduction paths between the evaporator and condenser walls.
   - **Condenser temperature non-uniformity ΔT_c is non-monotonic**, reaching its minimum at the intermediate VC-14 ($\Delta T_c \approx 0.38$ °C), compared with ≈ 1.28 for VC-12 and ≈ 0.71 for VC-16. VC-14 thus offers the most uniform condenser surface, while VC-12 is the least uniform.

   Critically, the lowest R_{vc} of VC-16 is *not* evidence of superior two-phase performance. The steady-state vapor volume fraction falls in the same direction as the rib count — from 1.0 (VC-12) through 0.88 (VC-14) to ≈ 0.005 (VC-16) — showing that the denser arrays achieve their lower resistance by shifting from phase-change-dominated towards conduction-dominated operation. At 400 kW/m^2 the VC-16 layout no longer sustains an active vapor phase and effectively behaves as a solid metallic spreader. The choice of rib count is therefore a trade-off between minimising R_{vc} (favouring more ribs), minimising ΔT_c (favouring the intermediate VC-14), and preserving the phase-change cycle the device is designed to exploit (favouring fewer ribs, VC-12).

3. For the VC-12 configuration — the only one that operates as a fully developed vapor chamber across the tested range — the medium heat flux of approximately 400 kW/m^2 represents the optimal operating regime: below this level (80 kW/m^2) phase change fails to initiate (VF oscillates near zero) and the latent-heat capability is not utilised; above it (800 kW/m^2) the system approaches its critical heat flux limit and reliability is compromised. The recommended safe operating range for VC-12 lies between approximately 200 and 600 kW/m^2.

5 Discussion

The results from the model verification, the comparison across rib configurations, and the heat flux parametric study are discussed here.

5.1 Verification of the Model through the No-Rib Case

In the absence of dedicated experimental data, the VC-N case serves as a reverse-validation of the developed CFD model. As shown in Figure 10, the maximum wick temperature climbs from 26.85 ℃ and stabilises at approximately 197 ℃ after about 30 s, while the average vapor-core temperature remains at its initial level throughout. The chamber reaches

a steady state, but a degenerate, conduction-only one in which the evaporator overheats because the phase-change cycle is never established.

The combination of a runaway wick temperature, a thermally inactive vapor core (Figure 10), and a vapor volume fraction that saturates only through boil-off rather than through a closed circulation confirms that no evaporation–condensation cycle is established, which is consistent with the expected behaviour of an unsupported ultra-thin vapor chamber under high vacuum and high heat flux. The result thus reproduces the loss-of-two-phase-operation failure mode anticipated from Jiang et al. [19], supporting the conclusion that the present model correctly captures the coupling between capillary transport, phase change, and heat conduction.

This form of indirect verification has clear limitations compared with quantitative validation against experimental measurements. The model is shown to capture the correct qualitative failure mode but its quantitative accuracy in regimes far from dryout cannot be established by the VC-N case alone. This limitation is revisited in Section 5.5.

5.2 Influence of Rib Configuration

Comparing the steady-state results across the three configurations at 400 kW/m^2, two trends emerge that run in *opposite* directions and that must therefore be read together rather than in isolation. First, both the peak wick temperature and the overall thermal resistance decrease monotonically as the rib count increases: the peak wick temperature falls from approximately 163.8 °C in VC-12 to 94.4 °C in VC-14 and 44.8 °C in VC-16, while the thermal resistance follows the same ordering, $R_{vc} \approx 0.0080$, 0.0046 and 0.0032 °C/W respectively. Taken on their own, these numbers would suggest that a denser rib array is thermally superior, in line with the observation of Jiang et al. [19] that support structures act as preferential heat-conduction paths.

Second, and decisively, the steady-state vapor volume fraction falls in exactly the same direction as the rib count. VC-12 reaches full saturation (VF = 1.0), VC-14 attains only partial saturation (VF ≈ 0.88), and VC-16 never establishes a vapor phase at all (VF ≈ 0.005). This inverse coupling is the central result of the comparison: the low peak temperature and low thermal resistance of VC-16 are *not* evidence of superior two-phase performance, but a consequence of the chamber operating in a conduction-dominated regime. With the largest number of porous copper ribs spanning the vapor core, VC-16 provides so many parallel solid-conduction paths between the evaporator and condenser walls that heat is removed by conduction before the wick can reach the conditions required to sustain evaporation. At 400 kW/m^2 it therefore behaves essentially as a near-solid metallic spreader—heat being conducted through the aluminium envelope and the copper wick–rib skeleton—rather than as an active vapor chamber, and its very small vapor-core pressure drop (~8.6×10^{-5} Pa) reflects a near-stagnant core rather than an efficiently flowing one.

The same ribs that conduct heat efficiently also obstruct the vapor flow, as shown by the bluff-body wake patterns in Figure 16: the denser VC-16 array constrains the central vapor channel and produces more pronounced wakes, whereas the wider channel of VC-12 sustains a genuine vapor circulation at low flow resistance. The design choice is therefore not a search for a single "best" configuration, but a three-way trade-off between competing objectives: minimising the thermal resistance R_{vc} favours more ribs (VC-16); minimising the condenser-surface non-uniformity ΔT_c favours the intermediate VC-14 ($\Delta T_c \approx 0.38$ °C, against ≈ 1.28 °C for VC-12 and ≈ 0.71 °C for VC-16); and preserving the phase-change cycle

that the device is fundamentally designed to exploit favours fewer ribs (VC-12). Within the tested range, VC-12 is the only configuration that remains an active vapor chamber at the medium and high heat-flux levels, which is also why it exhibits the highest evaporator-side temperature: its latent-heat transport is active and the device is loaded close to its working point.

5.3 Influence of Heat Flux on Operating Regime

The three heat flux levels investigated for the VC-12 configuration reveal three distinct operating regimes, as summarised in Table 8 and visualised in Figure 23.

Table 8: Operating regimes of the VC-12 configuration at the three tested heat-flux levels.

Heat flux [kW/m^2]	80	400	800
Vapor volume fraction (steady)	≈0 (0.001–0.009)	1.0	1.0
$T_{\text{wick,max}}$ [°C]	50.0	163.8	301.0
T_{vapor} [°C]	47.1	145.0	263.3
Wick–vapor ΔT [K]	≈3	≈19	≈38
Vapor-core ΔP_{vc} [Pa]	2.5	0.06	0.001
Regime	Conduction-dominated	Optimal phase-change	Near-critical

5.3.1 The Low-Flux Conduction-Dominated Regime

At 80 kW/m^2, the vapor volume fraction oscillates between approximately 0.001 and 0.009 throughout the simulation, never reaching saturation. The wick–vapor temperature difference remains small (approximately 3 K), indicating that the latent heat of vaporisation is barely engaged. In this regime, heat transfer is governed primarily by solid and liquid conduction, and the temperature uniformity advantage of two-phase vapor spreading is not realised. This finding is consistent with the conclusion of Jiang et al. [19] that, at low input power, heat transfer is controlled by solid conduction through the support columns and the overall thermal resistance is relatively large.

5.3.2 The Medium-Flux Optimal Regime

At 400 kW/m^2, the vapor volume fraction rises to saturation within approximately 3 s and remains stable thereafter, while the pressure drop across the vapor core stays below 0.06 Pa. The wick–vapor temperature difference of approximately 19 K reflects a well-established phase-change cycle with effective latent heat utilisation. This regime corresponds to the intended operating mode of the vapor chamber: phase change is fully developed, pressure drop is low, and the temperature gradient between phases is moderate.

The identification of 400 kW/m^2 as “optimal” should be understood in the context of the three discrete points tested. The judgement is based on three simultaneous criteria: (i) the vapor volume fraction reaches saturation, confirming that latent heat transport is active; (ii) the wall temperature remains within the safe operating range of typical electronic devices; and (iii) the pressure drop is sufficiently small compared with the capillary pressure limit. Among the three tested heat fluxes, only 400 kW/m^2 satisfies all three criteria simultaneously. A more refined determination of the optimal operating point

would require additional intermediate cases (e.g. 200, 300, 500, 600 kW/m^2), which are recommended as future work.

5.3.3 The High-Flux Near-Critical Regime

At 800 kW/m^2, the vapor volume fraction saturates almost instantaneously, but the peak wick temperature reaches approximately 301 °C and the wick–vapor temperature difference widens to approximately 38 K. These values significantly exceed the safe operating range of consumer electronics, and indicate that the system is approaching its critical heat flux (CHF) limit. The fact that VC-12 sustains steady-state operation at 400 kW/m^2 but exhibits near-critical behaviour at 800 kW/m^2 suggests that the CHF of this configuration lies between these two values. A precise determination of the CHF would require additional simulations in the 500–800 kW/m^2 range and is recommended as future work. Based on the present three points and the additional consideration of safety margin, Since only 400 kW/m^2 was simulated within this interval, the bounds are inferred rather than directly resolved: the lower bound reflects the threshold below which phase change fails to initiate (as observed at 80 kW/m^2), and the upper bound is set conservatively below the near-critical behaviour seen at 800 kW/m^2. On this basis, a preliminary safe operating window for VC-12 is suggested to be approximately 200–600 kW/m^2, to be refined by future intermediate-flux cases.

5.4 Comparison with the Reference Study

The comparison with Jiang et al. [19] summarised in Table 9 reveals both convergent and divergent findings.

On the convergent side, both studies demonstrate that the number, arrangement, and shape of support structures exert a strong coupled influence on the thermal-hydraulic performance of vapor chambers by simultaneously regulating heat conduction paths and vapor flow channels. Within the rib-count range examined here (12–16), both studies are consistent in showing that a denser support array lowers the vapor-chamber thermal resistance; in the present simulations this improvement is monotonic, the densest VC-16 layout performing best. The associated narrowing of the vapor channel is the trade-off that would eventually cap the benefit at rib densities higher than those tested, but no such reversal occurs within the present range.

On the divergent side, the two studies differ in two important respects. First, the support structure form is different: Jiang et al. used discrete cylindrical columns including composite (solid core with porous outer layer) designs, whereas the present work uses square ribs treated as a single porous medium. Second, the optimisation strategies differ: Jiang et al. focused on adding multi-artery columns and grooved surfaces to enhance capillary transport, whereas the present work focuses on selectively removing redundant ribs to widen the vapor channel. These two approaches address the same trade-off (mechanical support versus vapor flow resistance) from opposite ends, and a combined strategy that simultaneously optimises rib distribution and incorporates grooved surfaces could be a productive direction for future work.

Table 9: Comparison of key findings between the present study and Jiang et al. [19].

Dimension	**Jiang et al. (composite columns, 25→225)**	**Present study (VC-12→VC-16)**
Number effect	Column count ↑ → R_{vc} ↓ 14.5%, ΔT_c ↑ 34.9%	Rib count ↑ (12→16) → R_{vc} ↓ from 0.0080 to 0.0032 ℃/W (≈60%) and peak wick temperature ↓ from 163.8 to 44.8 ℃, *but* vapor volume fraction ↓ from 1.0 to ≈0.005
Flow features	Dense columns → vapor velocity ↑ 161%	Dense ribs → constrained vapor channel, pronounced wake
Operating regime	Diagonal distribution with multi-artery columns (VC-M)	No single optimum: VC-16 gives the lowest R_{vc} but reverts to solid conduction (VF≈0.005); VC-12 is the only configuration that stays an active vapor chamber. Rib count is a trade-off, not a maximisation
Failure mode	Dryout	Dryout: degenerate conduction-only steady state in the no-rib (VC-N) case (no closed two-phase cycle; wall ≈197 ℃)

R_{vc}: 0.0080 → 0.0046 → 0.0032 ℃/W; peak wick temperature: 163.8 → 94.4 → 44.8 ℃; vapor volume fraction: 1.0 → 0.88 → 0.005 (VC-12→VC-14→VC-16, all at 400 kW/m^2).

5.5 Limitations of the Numerical Methodology

Because no direct experimental validation has been performed in the present study, it is particularly important to discuss the sources of numerical uncertainty in the model. Four aspects deserve consideration.

5.5.1 Sensitivity to the Lee Model Coefficients

The evaporation and condensation intensity coefficients r_e and r_c in the Lee model are not measurable physical quantities but numerical parameters that control the sharpness of the predicted interface. In this study, both coefficients were set to 0.1 s^{-1} following the values reported by Rahmatullah and Wen [15]. However, values reported in the literature span more than three orders of magnitude (from 0.1 to 100 s^{-1}), and the choice can influence both numerical stability and the predicted onset of phase change. A systematic sensitivity analysis of the Lee coefficients was not performed in this work and is recommended for future studies aiming to establish quantitative accuracy.

A further manifestation of this coefficient dependence is the short start-up transient seen in the VC-N vapor-core temperature (Section 4.1.1), where the vapor temperature briefly dips below its initial value before recovering. Such short-lived over-/under-shoots in the interfacial energy balance are a known behaviour of the Lee source term when the phase-change rate is evaluated on a coarse start-up field, and become more pronounced as r_e and r_c increase. Because the transient decays within the first few time steps and all conclusions here are drawn from the steady-state fields, it does not affect the reported results; it does, however, reinforce the recommendation that r_e and r_c be swept systematically before any quantitative claim is made about the start-up dynamics.

5.5.2 Fixed Saturation Temperature Assumption

The saturation temperature inside the vapor chamber was held constant at 50 °C throughout all simulations. In reality, the saturation temperature varies with local pressure through the Clausius–Clapeyron relation. Under the medium heat flux of 400 kW/m^2, the vapor core pressure drop is only 0.06 Pa, so the assumption introduces negligible error. However, under the low heat flux of 80 kW/m^2, the pressure drop reaches 2.5 Pa, and the assumption may introduce a more noticeable bias in the predicted saturation behaviour. In high pressure drop regimes, a pressure-dependent saturation temperature would yield a more accurate prediction.

5.5.3 Mesh Independence and Domain Simplification

The mesh sensitivity study (Section 3.7) showed that, beyond approximately $1{\times}10^5$ cells, the predicted reference temperature remains within a narrow band of 47.3–47.7 °C (Figure 43). The chosen medium mesh therefore produces results within approximately 1% of the fine-mesh solution for the key output quantities, which is considered acceptable for engineering analysis. However, the quarter-domain simplification assumes perfect geometric and thermal symmetry, which precludes capturing any asymmetric flow features that may arise in a full-domain simulation. Additional simplifications include the neglect of non-condensable gas accumulation, manufacturing-induced wick non-uniformity, and working-

fluid degradation effects, all of which would be relevant for long-term operation of real devices.

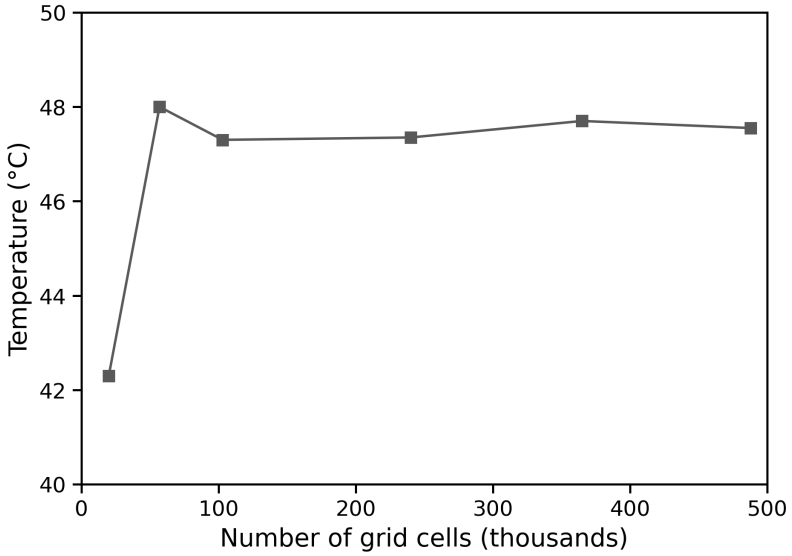


Figure 43: Grid independence study: the reference temperature as a function of the number of mesh cells. The solution becomes essentially mesh-independent beyond approximately 1×10^5 cells.

5.5.4 Treatment of the Support Ribs

A further modelling assumption concerns the treatment of the support ribs. Here the ribs are modelled as a fully porous copper medium with a permeability ($K = 1.0 \times 10^{-8}$ m^2) three orders of magnitude higher than the wick, so they act not only as mechanical supports but also as an auxiliary liquid-return network bridging the upper and lower wicks across the vapor core. Real anti-collapse structures are often solid (mechanical support only), with only composite solid-core/ porous-shell designs contributing to capillary return. Treating every rib as fully porous therefore likely amplifies their liquid-return benefit and is one reason the no-rib case fails so completely: removing the ribs removes both the mechanical support and a substantial part of the cross-core return capacity. The qualitative trade-off identified in this study is unaffected, but the penalty for removing ribs would be smaller if the ribs were modelled as partly or wholly solid.

5.5.5 Implications for the Quantitative Accuracy of the Results

Taken together, these limitations imply that the quantitative values presented in this work, particularly the absolute temperatures at high heat flux and the precise CHF estimate, should be interpreted as indicative rather than definitive. The trends and qualitative conclusions—namely that increasing rib count (VC-16) gives the lowest peak temperature and thermal resistance, that 400 kW/m^2 is the optimal operating regime for the VC-12 configuration, and that the no-rib case fails through dryout—are expected to be robust against these uncertainties, since they reflect underlying physical mechanisms that the model demonstrably captures. The precise quantitative values, however, would benefit from future validation against either experimental data or higher-fidelity numerical simulations.

6 Concluding Remarks

In conclusion, this thesis successfully addressed both goals of first developing a CFD methodology for porous rib structures in ultra-thin vapor chambers and then investigating the change in thermal-hydraulic performance when varying the number and arrangement of support ribs and the operating heat flux.

The development of the CFD methodology combined a three-dimensional transient solver with the Brinkman–Forchheimer extended Darcy model for porous wick flow and the Lee phase-change model provided by ANSYS Fluent's built-in evaporation–condensation model. In the absence of dedicated experimental data, the no-rib baseline (VC-N) was used as a reverse-validation case. The simulation correctly captured the failure mode expected for an unsupported chamber: rather than establishing a two-phase cycle, the wick temperature rose to a steady value of approximately 197 °C and boiled off the local liquid, while the vapor-core temperature remained stagnant and the vapor never circulated, so heat was ultimately removed by lateral solid conduction alone—the signature of dryout. This behaviour confirms that the model correctly couples capillary transport, phase change, and heat conduction, and that support structures are mechanically and thermally indispensable in ultra-thin vapor chamber designs. The quarter-domain simplification, the fixed saturation temperature, and the choice of Lee model coefficients were identified as the main sources of numerical uncertainty, and limit the quantitative accuracy of the absolute values predicted at high heat flux. The qualitative trends and the identified operating regimes, however, are expected to be robust against these uncertainties because they reflect underlying physical mechanisms that the model demonstrably captures.

The parametric investigation into rib configuration and heat flux yielded several insights into the thermal-hydraulic behaviour of porous rib structures. Comparing VC-16, VC-14 and VC-12 at 400 kW/m^2, the wall-temperature distribution showed a characteristic "X"-shaped pattern of elevated temperature in VC-12, concentrated over the heat source and in the gaps between adjacent ribs, whereas VC-16 exhibited the most uniform field with the lowest peak temperature. This pattern confirmed that the ribs act as preferential heat-conduction paths but simultaneously obstruct vapor flow through bluff-body wake formation. Both the peak wick temperature and the thermal resistance decreased monotonically with rib count (from 163.8 ℃ and 0.0080 ℃/W for VC-12 to 44.8 ℃ and 0.0032 ℃/W for VC-16). Crucially, however, the steady-state vapor volume fraction fell in the same direction, from 1.0 (VC-12) through 0.88 (VC-14) to approximately 0.005 (VC-16). The lower temperature and resistance of the denser arrays are therefore obtained by shifting the chamber from phase-change-dominated towards conduction-dominated operation, rather than by improving its two-phase performance: at 400 kW/m^2 VC-16 no longer sustains an active vapor phase and effectively behaves as a near-solid metallic spreader. Removing four non-critical ribs to form VC-12 widened the central vapor channel from approximately 5.8 mm to 26 mm and is what preserves an active phase-change cycle at the medium and high heat fluxes (400 and 800 kW/m^2), while ensuring the chamber never reverts to the dry, degenerate state of VC-N at any tested flux; the accompanying rise in peak temperature and in condenser non-uniformity is the price of keeping the vapor chamber active. The selection of rib count is thus a genuine trade-off between minimising thermal resistance (favouring more ribs), minimising condenser non-uniformity (favouring the intermediate VC-14, $\Delta T_c \approx 0.38$ ℃), and preserving the active vapor phase the device is designed to exploit (favouring the wider-channel VC-12) — and not a case of any single configuration being uniformly optimal.

The investigation of the operating heat flux for the VC-12 configuration revealed three distinct regimes. At 80 kW/m^2, the vapor volume fraction oscillated between approximately 0.001 and 0.009 throughout the simulation without ever reaching saturation, indicating that the latent heat of vaporisation was not engaged and that heat transfer was governed by solid and liquid conduction. At 400 kW/m^2, the vapor volume fraction stabilised at unity within approximately 3 s, the pressure drop across the vapor core remained below 0.06 Pa, and the wick–vapor temperature difference settled at approximately 19 K, all of which indicate a well-established two-phase circulation cycle. At 800 kW/m^2, the peak wick temperature reached approximately 301 ℃ and the wick–vapor temperature difference widened to approximately 38 K, signalling that the system was approaching its critical heat flux limit. Based on these three points, the critical heat flux of the VC-12 configuration was inferred to lie between 400 and 800 kW/m^2, and the recommended safe operating range was identified as approximately 200–600 kW/m^2.

A crucial note for both the rib configuration comparison and the heat flux study is that the present simulations were performed on a symmetric quarter-domain with a single centred heat source. Real-world vapor chambers in high-performance computing applications typically experience non-uniform power maps, multiple discrete heat sources, and gravity effects that were not considered in this work. The optimal rib layout in such real-world scenarios would likely differ from the symmetric VC-12 configuration and would need to be tailored to the specific heat source distribution and operational orientation.

7 Perspectives

This thesis work is a numerical study of porous rib structures in ultra-thin vapor chambers, providing an overview of the trade-off between mechanical support and vapor flow obstruction, and identifying three distinct operating regimes based on the applied heat flux. The developed methodology serves as a starting point for the design of rib layouts in next-generation vapor chambers, and leaves several open questions for future investigation.

The most direct extension of the present work is experimental validation. The simulations performed here used the no-rib baseline as a reverse-validation case, which confirms that the model correctly captures the qualitative dryout failure mode but does not establish quantitative accuracy in regimes far from dryout. A dedicated experimental campaign measuring the wall temperature distribution and the vapor core pressure drop on physical prototypes of VC-16, VC-12, and ideally additional rib configurations would substantially strengthen the conclusions. Infrared thermography of the condenser surface and embedded pressure sensors in the vapor core, combined with controlled heat flux input, would provide the data needed to quantify the model error and to refine the choice of the Lee model coefficients.

The precise determination of the critical heat flux (CHF) for the VC-12 configuration is another important follow-up. The present study identified that the CHF lies between 400 and 800 kW/m^2 based on three discrete heat flux points, but the exact value and the corresponding failure mechanism remain to be resolved. Additional simulations at intermediate heat flux levels (e.g. 500, 600, 700 kW/m^2), combined with refined diagnostics of the local wick saturation and vapor velocity near the heat source, would allow a more precise CHF prediction and identification of whether dryout occurs through capillary limit or boiling-induced wick depletion.

A systematic sensitivity analysis of the Lee model coefficients (r_e and r_c) would also be valuable. In this work, both coefficients were fixed at 0.1 s^{-1} based on literature recommendation, but values reported in the literature span more than three orders of magnitude. Sweeping these coefficients across the literature range while monitoring steady-state thermal resistance, pressure drop, and time to reach steady state would clarify the sensitivity of the predicted regimes to this numerical parameter and would provide a more rigorous basis for the model's quantitative claims.

The parametric study in this thesis varied only the rib number and the heat flux. The design space of porous rib structures, however, also includes rib thickness, cross-sectional shape, spatial arrangement, and the distinction between solid and porous rib cores. Following the work of Jiang et al., who demonstrated that composite columns with a solid core and a porous outer layer reduce liquid pressure drop while maintaining mechanical strength, a natural extension is to investigate composite rib structures within the present framework. Similarly, incorporating graded microgrooves on the rib surfaces, as proposed by Xie et al., would allow direct comparison between rib-reduction (the strategy of the present work) and capillary-enhancement (the strategy of these prior studies) approaches to vapor chamber optimisation.

The present geometry assumes a single centred heat source and a symmetric quarter-domain. Real-world chips, however, exhibit highly non-uniform power maps with multiple discrete hotspots that vary depending on workload. A future study could simulate full-domain geometries with realistic multi-hotspot power distributions and investigate whether the optimal rib layout becomes asymmetric, with locally denser rib placement near high-power regions and sparser placement elsewhere. This direction is particularly relevant for smartphone and laptop applications where the chip power distribution is well-characterised but rarely uniform.

Finally, the present model neglects non-condensable gas accumulation and long-term wick degradation. While these simplifications are reasonable for short-duration thermal-hydraulic analysis, they limit the model's applicability to reliability and lifetime predictions. Modelling non-condensable gas accumulation would enable prediction of long-term performance degradation, which is one of the dominant failure modes in commercial vapor chambers. These extensions, combined with experimental validation, would move the methodology from a research tool towards an industrial design tool for next-generation thermal management solutions.

References

[1] R. S. Gaugler, "Heat transfer device." U.S. Patent No. 2,350,348, 1944. Filed 21 December 1942, published 6 June 1944.

[2] G. M. Grover, T. P. Cotter, and G. F. Erickson, "Structures of very high thermal conductance," *Journal of Applied Physics*, vol. 35, no. 6, pp. 1990–1991, 1964.

[3] Y. T. Chen, S. W. Kang, Y. H. Hung, C. H. Huang, and K. C. Chien, "Feasibility study of an aluminum vapor chamber with radial grooved and sintered powders wick structures," *Applied Thermal Engineering*, vol. 51, no. 1–2, pp. 864–870, 2013.

[4] A. Faghri, "Heat pipes: Review, opportunities and challenges," *Frontiers in Heat Pipes*, vol. 5, no. 1, p. 1, 2014.

[5] S. V. Garimella and C. B. Sobhan, "Transport in microchannels – a critical review," *Annual Review of Heat Transfer*, vol. 13, pp. 1–50, 2003.

[6] Y. Tang, R. Zhou, L. Lu, Y. Xie, and W. Zhou, "Advancements and challenges in ultra-thin vapor chambers for high-efficiency electronic thermal management: A comprehensive review," *International Journal of Heat and Mass Transfer*, vol. 224, p. 125393, 2024.

[7] Z. Chen, Y. Li, W. Zhou, L. Deng, and Y. Yan, "Design, fabrication and thermal performance of a novel ultra-thin vapor chamber for cooling electronic devices," *Energy Conversion and Management*, vol. 187, pp. 221–231, 2019.

[8] R. Li, Y. Gan, Q. Luo, Y. Yan, and Y. Li, "Numerical analysis on thermal hydraulic characteristics of mesh-type ultra-thin vapor chambers," *Applied Thermal Engineering*, vol. 236, p. 121648, 2024.

[9] J. Zeng, L. Lin, Y. Tang, Y. Sun, and W. Yuan, "Fabrication and thermal performance of an ultra-thin vapor chamber with a novel composite wick," *Applied Thermal Engineering*, vol. 121, pp. 425–433, 2017.

[10] Z. Chen, Y. Li, J. Yu, L. Deng, H. Chen, X. Tang, and Y. Yan, "Fabrication and characterization of ultra-thin vapor chambers with printed wick structure," *International Communications in Heat and Mass Transfer*, vol. 121, p. 105113, 2021.

[11] G. Patankar, J. A. Weibel, and S. V. Garimella, "Patterning the condenser-side wick in ultra-thin vapor chamber heat spreaders to improve skin temperature uniformity of mobile devices," *International Journal of Heat and Mass Transfer*, vol. 101, pp. 927–936, 2016.

[12] D. A. Reay, P. A. Kew, and R. J. McGlen, *Heat Pipes: Theory, Design and Applications*. Oxford: Butterworth-Heinemann, 6 ed., 2014.

[13] Y. S. Chen, K. H. Chien, T. C. Hung, C. C. Wang, Y. M. Ferng, and B. S. Pei, "Numerical simulation of a heat sink embedded with a vapor chamber and calculation of effective thermal conductivity of a vapor chamber," *Applied Thermal Engineering*, vol. 29, no. 13, pp. 2655–2664, 2009.

[14] R. Ranjan, J. Y. Murthy, S. V. Garimella, D. H. Altman, and M. T. North, "Modeling and design optimization of ultrathin vapor chambers for high heat flux applications," *IEEE Transactions on Components, Packaging and Manufacturing Technology*, vol. 2, no. 9, pp. 1465–1479, 2012.

[15] Y. Rahmatullah and T. Y. Wen, "Lee model based numerical scheme for steady vapor chamber simulations," *International Journal of Heat and Mass Transfer*, vol. 201, p. 123636, 2023.

[16] Y. Rahmatullah and T. Y. Wen, "Optimization of thermal-hydraulic performance for pillar-reinforced vapor chamber using Lee model based numerical scheme and analysis of variance," *International Communications in Heat and Mass Transfer*, vol. 152, p. 107319, 2024.

[17] X. Xie, Z. Cao, J. He, H. Liao, and Y. Huang, "Thermal performance analysis of supporting column ultra-thin vapor chamber with graded microgroove," *Applied Thermal Engineering*, vol. 258, p. 124578, 2025.

[18] S. Sudhakar, J. A. Weibel, and S. V. Garimella, "A methodology to predict the power dissipation limits of high-heat-flux vapor chambers considering boiling in the evaporator," *International Journal of Heat and Mass Transfer*, vol. 253, p. 127622, 2025.

[19] H. Jiang, X. Wang, Z. Xu, H. Qi, D. Shan, B. Guo, and J. Xu, "Numerical analysis of support column manipulation for efficient heat transfer in vapor chambers," *International Journal of Heat and Mass Transfer*, vol. 253, p. 127520, 2025.

[20] H. K. Versteeg and W. Malalasekera, *An Introduction to Computational Fluid Dynamics: The Finite Volume Method*. Harlow, UK: Pearson Education, 2nd ed., 2007.

[21] F. P. Incropera, D. P. DeWitt, T. L. Bergman, and A. S. Lavine, *Fundamentals of Heat and Mass Transfer*. Hoboken: John Wiley & Sons, 8 ed., 2017.

[22] K. Vafai, ed., *Handbook of Porous Media*. Boca Raton: CRC Press, 3 ed., 2015.

[23] D. A. Nield and A. Bejan, *Convection in Porous Media*. Cham, Switzerland: Springer, 5th ed., 2017.

[24] S. Ergun, "Fluid flow through packed columns," *Chemical Engineering Progress*, vol. 48, no. 2, pp. 89–94, 1952.

[25] W. H. Lee, "A pressure iteration scheme for two-phase flow modeling," in *Multiphase Transport: Fundamentals, Reactor Safety, Applications* (T. N. Veziroglu, ed.), pp. 407–432, Washington, D.C.: Hemisphere Publishing, 1980.

[26] D. L. Sun, J. L. Xu, and L. Wang, "Development of a vapor–liquid phase change model for volume-of-fluid method in FLUENT," *International Communications in Heat and Mass Transfer*, vol. 39, no. 8, pp. 1101–1106, 2012.

[27] C. R. Kharangate and I. Mudawar, "Review of computational studies on boiling and condensation," *International Journal of Heat and Mass Transfer*, vol. 108, pp. 1164–1196, 2017.

[28] ANSYS, Inc., Canonsburg, PA, *ANSYS Fluent Theory Guide*, 2022.